

9

10

11 **Fracturing and healing of basaltic magmas during explosive volcanic eruptions**

12

13 J. Taddeucci<sup>1#</sup>, C. Cimarelli<sup>2</sup>, M.A. Alatorre-Ibarguenuoitia<sup>3</sup>, H. Delgado-Granados<sup>4</sup>, D. Andronico<sup>5</sup>,  
14 E. Del Bello<sup>1</sup>, P. Scarlato<sup>1</sup>, F. Di Stefano<sup>1</sup>

15

16 1) Istituto Nazionale di Geofisica e Vulcanologia, Roma<sup>1</sup>, Via di Vigna Murata 605, 00143, Rome,  
17 Italy. #Corresponding Author (jacopo.taddeucci@ingv.it)

18 2) Department of Earth and Environmental Sciences, Ludwig-Maximilians-Universität München.  
19 Theresienstrasse 41, 80333 Munich, Germany.

20 3) Instituto de Investigación en Gestión de Riesgo y Cambio Climático, Universidad de Ciencias y  
21 Artes de Chiapas, Libramiento Norte poniente 1150, Lajas Maciel, 29039, Tuxtla Gutiérrez, Mexico

22 4) Departamento de Vulcanología, Instituto de Geofísica, Universidad Nacional Autónoma de México  
23 Circuito Exterior, C. U. Coyoacán 04510, Mexico City, Mexico

24 5) Istituto Nazionale di Geofisica e Vulcanologia, Osservatorio Etneo - Sezione di Catania, Piazza  
25 Roma 2, 95125 Catania, Italy.

26 **Main text**

27 **The eruption of basaltic magmas dominates explosive volcanism on Earth and other planets**  
28 **within the Solar System. The mechanism through which continuous magma fragments into**

volcanic particles is central in governing eruption dynamics and the ensuing hazards. However, the mechanism of fragmentation of basaltic magmas is still disputed, with both viscous and brittle mechanisms having been proposed. Here we carry out textural analysis of the products of ten eruptions from seven volcanoes by Scanning Electron Microscope. We find broken crystals surrounded by intact glass that testify to the brittle fragmentation of basaltic magmas during explosive activity worldwide. We then replicated the natural textures of broken crystals in laboratory experiments where variably crystallised basaltic melt was fragmented by rapid deformation. The experiments reveal that crystals are broken by the propagation of a network of fractures through magma, and that afterwards the fractures heal by viscous flow of the melt. Fracturing and healing affect gas mobility, stress distribution, and bubble and crystal size distributions in magma. Our results challenge the idea that the grain size distribution of basaltic eruption products reflects the density of fractures that initially fragmented the magma and ultimately indicate that brittle fracturing and viscous healing of magma may underlie basaltic explosive eruptions globally.

The eruption of fragmental magma of basaltic composition is the most frequent type of explosive volcanism on Earth and in the Solar System<sup>1-3</sup>. Eruptions span from centuries of persistent, weak explosions, through days to months of lava fountains and ash emissions, to rare, global-scale catastrophic events<sup>4,5</sup>. Explosive eruptions occur when continuous magma is fragmented into volcanic particles – or pyroclasts. Fragmentation boosts the expansion of the gas phase present in the magma, converting magma internal energy into eruptive kinetic energy and determining the size distribution and dispersal of pyroclasts<sup>2,6-8</sup>. In turn, these parameters critically determine the hazards posed by explosive eruptions, from the life-claiming fallout of volcanic bombs close to the volcano<sup>9,10</sup> to the regional-scale atmospheric dispersal of volcanic ash and its impact on air traffic, public health, infrastructures, and climate<sup>11-14</sup>.

While several criteria exist for the fragmentation of more viscous magmas<sup>15–19</sup>, the fragmentation of basaltic magmas is still hotly debated. It has often been attributed to the viscous thinning of magma by fluid-dynamic instabilities<sup>8,20–22</sup>, but also to the brittle failure of magma without appreciable viscous deformation, mainly in eruptions driven by magma-water interaction<sup>23</sup> or crystal-rich magmas in violent eruptions<sup>2,23–27</sup>. Energetic considerations and clast morphology suggest that basaltic ash particles may result from brittle fragmentation<sup>28–30</sup>, but textural evidences may also record later-stage processes overprinting the original fragmentation, including particle collision and recycling inside volcanic vents<sup>31</sup>. Uncertainties as to which fragmentation criterion is more appropriate for basaltic magmas, or if a single criterion can satisfy their broad spectrum of eruption styles, are hindering our capability to understand and model basaltic explosive volcanism on Earth and elsewhere.

Here we demonstrate that broken crystals found inside basaltic pyroclasts offer robust proof for the brittle fragmentation of basaltic magmas. Features of these broken crystals are reproduced experimentally, revealing that fragmentation occurs through the propagation of a network of branching fractures during rapid deformation of magma. Both in the experiments and in nature, fracturing is followed by viscous healing which masks the fractures, leaving broken crystals as the only preserved traces in the magma. We found broken crystals in the products of ten eruptions spanning a wide range of activity style and magma composition, indicating that brittle fracturing and viscous healing of basaltic magmas is common over the entire spectrum of eruption explosivity.

### **Features of broken crystals in basalt**

Broken crystals of plagioclase, pyroxene, olivine, and Fe-Ti-oxides, 1–500  $\mu\text{m}$  in size, are ubiquitously found in the products of ten explosive eruptions encompassing styles from Strombolian to paroxysmal and violent Strombolian, with ash-poor to ash-rich plumes from 0.1 to 6 km high and magma discharge rates from  $10^2$  to  $10^6$   $\text{kg s}^{-1}$ , compositions from basanite to basaltic andesite, and crystallinity from 2 to

76 54 vol. % (see Methods and Extended Data Table 1). Broken crystals occur in millimetre-sized zones  
77 often localized at the margins of pyroclasts (Fig. 1, Extended Data Fig. 1a), but also, with no noticeable  
78 difference, as scattered individuals, appearing in ~10-20 % of the whole area investigated. They are  
79 found in pyroclasts from 10  $\mu\text{m}$  to 0.5 m across, but more commonly in ash-sized ( $< 2 \text{ mm}$ ) than lapilli-  
80 (2-64 mm) or bomb-sized ( $>64 \text{ mm}$ ) ones.

81 In general, broken crystals lie within an intact groundmass. Fractures in broken crystals can be glass-  
82 filled or open, with straight, curved, irregular, jigsaw, stepped, and branched morphologies and  
83 multiple fracture generations (Fig. 1a-d, Extended Data Fig. 2, and Supplementary Data 1 and 2). Open  
84 fractures range from small, rounded vesicles inside glass fillings, to irregular vesicles larger than the  
85 whole crystal (Fig. 1g-k). Fracture density can be  $>2 \times 10^3$  fractures per  $\text{mm}^2$  (Extended Data Fig. 1a),  
86 and varies from a single fracture per crystal, to fractures with micron- to sub-micron spacing in  
87 shattered crystals (Fig. 1f). Crystal fragments are displaced in all directions after fracturing, pulling  
88 apart being always evident in open fractures, and rotation being also common (Extended Data Fig. 1b,  
89 Extended Data Fig. 2g-j). Occasionally, flow banding of Fe-rich glass filaments evidences melt flow  
90 after fracturing (Extended Data Fig. 2f,g).

91 Open fractures occasionally extend beyond crystals and into the glass and even into vesicles, with  
92 smooth margins indicative of melt viscous flow after fracturing (Fig. 1m,n). Several such fractures are  
93 interconnected by Fe-rich glass filaments, remains of a longer fracture partially healed (Fig. 1l,m), as  
94 previously reported<sup>32</sup>. Extensive fracture healing leaves behind only an alignment of small vesicles,  
95 crystal fragments, and Fe-rich glass filaments (Fig. 1o and Extended Data Fig. 2e,f).

## 96 **Experimental constraints on the origin of broken crystals**

97 In order to understand the processes responsible for their formation, broken crystals were reproduced in  
98 laboratory fragmentation experiments following Büttner and co-authors<sup>33</sup> (Fig. 2). Basaltic pyroclasts

99 were melted in a steel crucible at 1275 °C and then left to crystallize for variable time at 1160 °C until  
100 obtaining variable degrees of crystallinity (3-63 vol. %, Extended Data Table 1). After cooling to 1080  
101 °C, similar to the eruptive temperature<sup>34</sup>, sudden injection of compressed Argon gas at the base of the  
102 sample caused its doming, fracturing, and fragmentation (see Supplementary Video 1). High-speed  
103 imaging (Fig. 2a-d) and calculations suggest maximum syn-fracturing elongation strain rates of the  
104 sample of  $10^2$ - $10^3$  s<sup>-1</sup> over length scales of a few millimetres<sup>33</sup>. Experimental fragments, microns to  
105 centimetres in size and fluidal to blocky in shape, display variable crystallinity, larger fragments  
106 retaining some of the fractures captured by high-speed imaging during deformation (Fig. 2e,f).

107 Near the sample surface, fractures display sharp, jagged outlines indicative of their brittle origin,  
108 transitioning into smooth, sinuous outlines due to viscous flow in the sample interior (Fig. 2f, Fig. 3a-e,  
109 and Extended Data Fig. 3a). Melt flowing into the fractures occasionally formed isolated vesicles (Fig.  
110 3a and Extended Data Fig. 3b,c) and vesicle alignments (Fig. 3f-I and Extended Data Fig. 3j).

111 In the products from all experiments, fractures and fracture-derived vesicles are surrounded, for some  
112 millimetres, by broken crystals otherwise missing elsewhere. Features of broken crystals are the same  
113 as in volcanic products, including open and glass-filled fractures and Fe-rich glass filaments (Fig. 3e-m  
114 and Extended Data Fig. 3g-o). Transitions among fractures, fracture-derived vesicles, and open and  
115 glass-filled fractures in broken crystals are abundant (Fig. 3c-e and Extended Data Fig. 3d-f). A  
116 hierarchy of fractures exists, their width and length decreasing away from the largest fractures.

117 Broken crystals are found in all experimental products, independent of sample zone (e.g., surface,  
118 interior, or periphery) and crystallinity differences. As in natural products, also in the experimental  
119 ones broken crystals and the associated textures are more abundant in smaller fragments and in  
120 fragment's periphery. Quantitative fracture parameters in natural and experimental products are nearly  
121 undistinguishable within their internal variability, fractures mostly ranging 0.02-10 µm in width, 0.2-

122 100  $\mu\text{m}$  in length, 1-100 in aspect ratio, 1-1.5 in tortuosity, and open fractures being larger than glass-  
123 filled ones (Fig. 4).

## 124 **Fracturing and healing of basaltic magmas**

125 Broken crystals in volcanic rocks have been previously attributed to multiple causes, including flow  
126 shear, shock wave and impact fragmentation, and brittle magma failure<sup>35-39</sup>. The transition that we  
127 observed between fractures in melt and in crystals cannot be explained by shear flow, which would  
128 break crystals without fracturing melt. Our fragmentation experiments illustrate effectively how the  
129 textures of broken crystals are formed by brittle fracturing. Gas injection from below imposes a  
130 complex stress field to the expanding sample, which undergoes brittle failure through the propagation  
131 of tensional fractures<sup>33</sup> (Fig. 2). These fractures form a branching network that cuts through the melt  
132 and breaks the crystals (Fig. 3). Matching parameters and textures in the experimental and natural  
133 products show that brittle fracturing occurs also in basaltic magmas during explosive eruptions. There,  
134 broken crystals form when a network of branching fractures propagates through magma, larger  
135 fractures bounding individual pyroclasts, smaller ones propagating only a short distance into magma  
136 (Fig. 5). Accordingly, broken crystals are more common in smaller particles and along the margins of  
137 larger ones, where fracture density in magma was higher. Analogies with the experimental products  
138 (Fig. 3k-m) and the presence of open fractures and elongation features (Fig. 1i,j,k) suggest that  
139 fragmenting magma undergoes rapid extension. This may occur repeatedly both inside and outside the  
140 volcanic conduit according to the specific dynamics of the different eruption styles. Magma ascent, gas  
141 pockets expansion, hydrodynamic instabilities, and drag with gas and air may all result in local stress  
142 and strain rate exceeding those required for brittle fracturing<sup>8,22,26,40</sup>. The strain rates in our experiments  
143 are a factor of two to three higher than those required for the brittle fracturing of basaltic melts at  
144 crystal volume fractions close to maximum packing<sup>26</sup> ( $\sim 1 \text{ s}^{-1}$ ), but both in the experiments and in

145 eruptions brittle fracturing occurred also at much lower crystal fractions (2-3 vol. %) as testified by the  
146 presence of broken crystals.

147 After fracturing, viscous flow of the melt heals — partially or completely — the fractures. Flow and  
148 healing must occur before the melt quenches below its glass transition temperature. The duration of the  
149 time interval between fracturing and cooling, and the local melt flow velocity, function of its viscosity,  
150 surface tension, and local pressure gradient, determine the maximum width of fractures that can be  
151 healed. Thinner fractures heal faster, leaving glass-filled broken crystals. Wider fractures heal slower  
152 and can leave open fractures in the crystals (Fig. 4).

153 The time elapsed between melt fracturing and quenching depends on the travel time of magma from its  
154 fracturing depth to its ejection and cooling into the atmosphere, function of clast size<sup>41</sup>. Fracturing  
155 depth, rise speed, and clast size thus determine the potential for the preservation of fractures in  
156 pyroclasts. The time scales relevant for our natural and experimental case studies are those for fracture  
157 propagation ( $<10^{-4}$  s), fracture healing by surface tension ( $10^{-4}$ -1 s), travel of the fractured magma  
158 before clast formation (0 to  $>10^3$  s) and from clast formation to ejection ( $10^{-2}$ -10 s), and cooling after  
159 ejection ( $1$ - $10^2$  s) (see Methods). Fractures larger than  $\sim 10$   $\mu\text{m}$  seem to effectively break magma into  
160 pyroclasts, because such fractures are rare in broken crystals (Fig. 4). If a  $10$   $\mu\text{m}$ -wide fracture requires  
161  $\sim 1$  s to heal, and pyroclasts travel at a velocity of  $\sim 100$   $\text{m s}^{-1}$  to the surface where they cool (see  
162 Methods), then pyroclast formation should occur at a depth that can be tentatively placed in the order of  
163  $100$  m or less. Deeper pyroclast formation would increase the chances of fractures larger than  $10$   $\mu\text{m}$   
164 being healed and preserved. Incomplete fracturing of magma may still occur at greater depth, but the  
165 resulting increased fracture healing and larger spreading of crystal fragments could render it hardly  
166 detectable, unless fractures were preserved by rapid quenching due to, e.g., in-conduit contact with  
167 external water<sup>32</sup>. To the extreme, complete healing in the conduit could result in fragmented magma

168 contributing to lava effusion, as suggested by textural evidence and modelling for more silicic  
169 eruptions<sup>39,42</sup>.

170 Magma fracturing and healing unavoidably impact eruption evolution and products. Added crystal  
171 fragments could increase magma viscosity and non-Newtonian behaviour<sup>43</sup>. Added fractures provide  
172 new pathways for magma outgassing<sup>24,32,44,45</sup> and new surface for volatile diffusion, thus favouring  
173 magma degassing. Healing fractures can trap small bubbles in magma and crystals<sup>46</sup>. Overall, the size  
174 distribution of both crystals and vesicles inside pyroclasts will be affected, thus impacting the results of  
175 two well-established forensic tools in volcanology<sup>47,48</sup>.

176 It is a long-standing paradigm that the size distribution of pyroclasts reflects the efficiency of magma  
177 fragmentation<sup>2</sup>, higher fragmentation energy leading to higher fracture density and inevitably to smaller  
178 pyroclasts<sup>49</sup>. Fracture healing implies that only a fraction of the fractures that propagate through  
179 magma, and of the energy consumed by fragmentation, contribute to the formation of new particles<sup>7</sup>.  
180 Many of the healed fractures in broken crystals are a few microns or less apart. If unhealed, such  
181 fractures would be prone to later reactivation during, e.g., collisions between pyroclasts, resulting in the  
182 formation of ash particles of comparable small size. Fracture healing may be a crucial factor in  
183 reducing the abundance of hazardous fine-grained ash particles in the products of basaltic explosive  
184 eruptions.

185 Despite having been previously suggested<sup>24,25,29,32</sup> and recently modelled<sup>26,27,30</sup> for specific cases, the  
186 generalised brittle fragmentation of basaltic magmas remained unproved so far. The broken crystals  
187 and accompanying textures that we found provide direct evidence in this regard. It is remarkable how  
188 the same fragmentation textures were found in ash- to bomb-sized products from ten eruptions that  
189 differ by magma composition, tectonic setting, and multiple orders of magnitude in the volume, mass  
190 ejection rate, dispersal, and average grain size distribution of erupted products. Similar textures, and



possibly also unrecognised broken crystals, appear in previous literature covering many other eruptions spanning Hawaiian lava fountains, catastrophic Plinian events, and more<sup>32,50–58</sup>. Fracturing and healing are common in silicic magmas<sup>17,39,59</sup>, but were not considered feasible in basaltic ones<sup>60</sup> until recently<sup>32</sup>. We conclude that brittle fragmentation and subsequent healing are not limited to magma-water-driven or catastrophic eruptions or the formation of basaltic ash, but are ubiquitous factors controlling basaltic explosive volcanism.

#### **Data availability**

A selection of 317 microphotographs detailing pyroclast textures related to the fracturing and healing of basaltic magmas in explosive volcanic eruptions and in fragmentation experiments is provided as Supplementary Information and is available at Mendeley Data, V1, doi: 10.17632/h5ynspf336.1, while the entire dataset of more than 2100 microphotographs is available upon request from J.T. The data used in Fig. 4 and Extended Data Fig. 1 and Extended Data Table 1 are available at Mendeley Data, V1, doi: 10.17632/38rss8f2yb.1 and presented in the Source data. Source data are provided with this paper.

#### **References**

1. Wilson, L. Volcanism in the solar system. *Nat. Geosci.* **2**, 389–397 (2009).
2. Gonnermann, H. M. Magma Fragmentation. *Annu. Rev. Earth Planet. Sci.* **43**, 431–458 (2015).
3. Papale, P. Global time-size distribution of volcanic eruptions on Earth. *Sci. Rep.* **8**, 1–11 (2018).
4. Houghton, B. F. & Gonnermann, H. M. Basaltic explosive volcanism: Constraints from deposits and models. *Chemie der Erde* **68**, 117–140 (2008).

- 211 5. Taddeucci, J., Edmonds, M., Houghton, B., James, M. R. & Vergnolle, S. Hawaiian and  
212 Strombolian Eruptions. *Encycl. Volcanoes* 485–503 (2015) doi:10.1016/b978-0-12-385938-9.00027-4.
- 213 6. Kueppers, U., Scheu, B., Spieler, O. & Dingwell, D. B. Fragmentation efficiency of explosive  
214 volcanic eruptions: A study of experimentally generated pyroclasts. *J. Volcanol. Geotherm. Res.* **153**,  
215 125–135 (2006).
- 216 7. Alatorre-Ibargüengoitia, M. A., Scheu, B., Dingwell, D. B., Delgado-Granados, H. &  
217 Taddeucci, J. Energy consumption by magmatic fragmentation and pyroclast ejection during Vulcanian  
218 eruptions. *Earth Planet. Sci. Lett.* **291**, 60–69 (2010).
- 219 8. Cashman, K. V & Scheu, B. Magmatic Fragmentation. in *The Encyclopedia of Volcanoes* 459–  
220 471 (Elsevier Inc., 2015). doi:10.1016/b978-0-12-385938-9.00025-0.
- 221 9. Alatorre-Ibargüengoitia, M. A., Delgado-Granados, H. & Dingwell, D. B. Hazard map for  
222 volcanic ballistic impacts at Popocatepetl volcano (Mexico). *Bull. Volcanol.* **74**, 2155–2169 (2012).
- 223 10. Oikawa, T. *et al.* Reconstruction of the 2014 eruption sequence of Ontake Volcano from  
224 recorded images and interviews the Phreatic Eruption of Mt. Ontake Volcano in 2014 5. *Volcanology.*  
225 *Earth, Planets Sp.* **68**, 68–79 (2016).
- 226 11. Cook, R. J., Barron, J. C., Papendick, R. I. & Williams, G. J. Impact on agriculture of the  
227 Mount St. Helens eruptions. *Science (80-. ).* **211**, 16–22 (1981).
- 228 12. Green, F. H. Y. *et al.* Is volcanic ash a pneumoconiosis risk ? *Nature* **293**, 216–217 (1981).
- 229 13. Alvarado, J. A. C. *et al.* Anthropogenic radionuclides in atmospheric air over Switzerland  
230 during the last few decades. *Nat. Commun.* **5**, 1–6 (2014).

- 231 14. Woolley-Meza, O., Grady, D., Thiemann, C., Bagrow, J. P. & Brockmann, D. Eyjafjallajökull  
232 and 9/11: The Impact of Large-Scale Disasters on Worldwide Mobility. *PLoS One* **8**, 1–7 (2013).
- 233 15. Dingwell, D. B. Volcanic dilemma: flow or blow. *Science* (80-. ). **273**, 1054–1055 (1996).
- 234 16. Zhang, Y. A criterion for the fragmentation of bubbly magma based on brittle failure theory.  
235 *Nature* **402**, 648–650 (1999).
- 236 17. Gonnermann, H. M. & Manga, M. Explosive volcanism may not be an inevitable consequence  
237 of magma fragmentation. *Nature* **426**, 432–435 (2003).
- 238 18. Spieler, O. *et al.* The fragmentation threshold of pyroclastic rocks. *Earth Planet. Sci. Lett.* **226**,  
239 139–148 (2004).
- 240 19. Cordonnier, B. *et al.* The viscous-brittle transition of crystal-bearing silicic melt: Direct  
241 observation of magma rupture and healing. *Geology* **40**, 611–614 (2012).
- 242 20. Namiki, A. & Manga, M. Transition between fragmentation and permeable outgassing of low  
243 viscosity magmas. *J. Volcanol. Geotherm. Res.* **169**, 48–60 (2008).
- 244 21. Pioli, L. & Harris, A. J. L. Real-time geophysical monitoring of particle size distribution during  
245 volcanic explosions at stromboli volcano (Italy). *Front. Earth Sci.* **7**, 1–13 (2019).
- 246 22. Jones, T. J., Reynolds, C. D. & Boothroyd, S. C. Fluid dynamic induced break-up during  
247 volcanic eruptions. *Nat. Commun.* **10**, 1–7 (2019).
- 248 23. Büttner, R., Dellino, P., Zimanowski, B. & Bu, R. Identifying magma – water interaction from  
249 the surface features of ash particles. **401**, 688–690 (1999).

- 250 24. Houghton, B. F. *et al.* The influence of conduit processes on changes in style of basaltic Plinian  
251 eruptions: Tarawera 1886 and Etna 122 BC. *J. Volcanol. Geotherm. Res.* **137**, 1–14 (2004).
- 252 25. Valentine, G. A., Krier, D., Perry, F. V. & Heiken, G. Scoria cone construction mechanisms,  
253 Lathrop Wells volcano, southern Nevada, USA. *Geology* **33**, 629–632 (2005).
- 254 26. Moitra, P., Gonnermann, H. M., Houghton, B. F. & Tiwary, C. S. Fragmentation and Plinian  
255 eruption of crystallizing basaltic magma. *Earth Planet. Sci. Lett.* **500**, 97–104 (2018).
- 256 27. Arzilli, F. *et al.* Magma fragmentation in highly explosive basaltic eruptions induced by rapid  
257 crystallization. *Nat. Geosci.* **12**, 1023–1028 (2019).
- 258 28. Zimanowski, B., Wohletz, K., Dellino, P. & Büttner, R. The volcanic ash problem. *J. Volcanol.*  
259 *Geotherm. Res.* **122**, 1–5 (2003).
- 260 29. Dellino, P. *et al.* Ash from the Eyjafjallajökull eruption (Iceland): Fragmentation processes and  
261 aerodynamic behavior. *J. Geophys. Res. Solid Earth* **117**, 1–10 (2012).
- 262 30. Dürig, T., Sonder, I., Zimanowski, B., Beyrichen, H. & Büttner, R. Generation of volcanic ash  
263 by basaltic volcanism. *J. Geophys. Res. Solid Earth* **117**, 1–8 (2012).
- 264 31. Polacci, M., Andronico, D., de' Michieli Vitturi, M., Taddeucci, J. & Cristaldi, A. Mechanisms  
265 of Ash Generation at Basaltic Volcanoes: The Case of Mount Etna, Italy. *Front. Earth Sci.* **7**, 193  
266 (2019).
- 267 32. Owen, J., Shea, T. & Tuffen, H. Basalt, Unveiling Fluid-filled Fractures, Inducing Sediment  
268 Intra-void Transport, Ephemeral: Examples from Katla 1918. *J. Volcanol. Geotherm. Res.* **369**, 121–  
269 144 (2019).

- 270 33. Büttner, R., Dellino, P., Raue, H., Sonder, I. & Zimanowski, B. Stress-induced brittle  
271 fragmentation of magmatic melts: Theory and experiments. *J. Geophys. Res. Solid Earth* **111**, 1–10  
272 (2006).
- 273 34. Taddeucci, J., Pompilio, M. & Scarlato, P. Conduit processes during the July-August 2001  
274 explosive activity of Mt. Etna (Italy): Inferences from glass chemistry and crystal size distribution of  
275 ash particles. *J. Volcanol. Geotherm. Res.* **137**, 33–54 (2004).
- 276 35. Bindeman, I. N. Fragmentation phenomena in populations of magmatic crystals. *Am. Mineral.*  
277 **90**, 1801–1815 (2005).
- 278 36. Kennedy, B. *et al.* Conduit implosion during Vulcanian eruptions. *Geology* **33**, 581–584 (2005).
- 279 37. Miwa, T. & Geshi, N. Decompression rate of magma at fragmentation: Inference from broken  
280 crystals in pumice of vulcanian eruption. *J. Volcanol. Geotherm. Res.* **227–228**, 76–84 (2012).
- 281 38. van Zalinge, M. E., Cashman, K. V. & Sparks, R. S. J. Causes of fragmented crystals in  
282 ignimbrites: a case study of the Cardones ignimbrite, Northern Chile. *Bull. Volcanol.* **80**, 22 (2018).
- 283 39. Kendrick, J. E. *et al.* Crystal plasticity as an indicator of the viscous-brittle transition in  
284 magmas. *Nat. Commun.* **8**, 1–12 (2017).
- 285 40. Taddeucci, J. *et al.* In-flight dynamics of volcanic ballistic projectiles. *Rev. Geophys.* **55**, 675–  
286 718 (2017).
- 287 41. Moitra, P., Sonder, I. & Valentine, G. A. Effects of Size and Temperature-Dependent Thermal  
288 Conductivity on the Cooling of Pyroclasts in Air. *Geochemistry, Geophys. Geosystems* **19**, 3623–3636  
289 (2018).

- 290 42. Wadsworth, F. B., Llewellyn, E. W., Vasseur, J., Gardner, J. E. & Tuffen, H. Explosive-effusive  
291 volcanic eruption transitions caused by sintering. *Sci. Adv.* **6**, 7940 (2020).
- 292 43. Del Gaudio, P., Ventura, G. & Taddeucci, J. The effect of particle size on the rheology of  
293 liquid-solid mixtures with application to lava flows: Results from analogue experiments. *Geochemistry,*  
294 *Geophys. Geosystems* **14**, 2661–2669 (2013).
- 295 44. Houghton, B. F., Wilson, C. J. N., Fierstein, J. & Hildreth, W. Complex proximal deposition  
296 during the Plinian eruptions of 1912 at Novarupta, Alaska. *Bull. Volcanol.* **66**, 95–133 (2004).
- 297 45. Polacci, M., Baker, D. R., Bai, L. & Mancini, L. Large vesicles record pathways of degassing at  
298 basaltic volcanoes. *Bull. Volcanol.* **70**, 1023–1029 (2008).
- 299 46. Lamur, A., Kendrick, J. E., Wadsworth, F. B. & Lavallée, Y. Fracture healing and strength  
300 recovery in magmatic liquids. *Geology* **47**, 195–198 (2019).
- 301 47. Cashman, K. V. & Marsh, B. D. Crystal size distribution (CSD) in rocks and the kinetics and  
302 dynamics of crystallization II: Makaopuhi lava lake. *Contrib. to Mineral. Petrol.* **99**, 292–305 (1988).
- 303 48. Baker, D. R. *et al.* A four-dimensional X-ray tomographic microscopy study of bubble growth  
304 in basaltic foam. *Nat. Commun.* **3**, 1–8 (2012).
- 305 49. Dürig, T. & Zimanowski, B. ‘Breaking news’ on the formation of volcanic ash: Fracture  
306 dynamics in silicate glass. *Earth Planet. Sci. Lett.* **335–336**, 1–8 (2012).
- 307 50. Polacci, M., Corsaro, R. A. & Andronico, D. Coupled textural and compositional  
308 characterization of basaltic scoria: Insights into the transition from Strombolian to fire fountain activity  
309 at Mount Etna, Italy. *Geology* **34**, 201–204 (2006).

- 310 51. Sable, J. E., Houghton, B. F., Del Carlo, P. & Coltelli, M. Changing conditions of magma  
311 ascent and fragmentation during the Etna 122 BC basaltic Plinian eruption: Evidence from clast  
312 microtextures. *J. Volcanol. Geotherm. Res.* **158**, 333–354 (2006).
- 313 52. Costantini, L., Houghton, B. F. & Bonadonna, C. Constraints on eruption dynamics of basaltic  
314 explosive activity derived from chemical and microtextural study: The example of the Fontana Lapilli  
315 Plinian eruption, Nicaragua. *J. Volcanol. Geotherm. Res.* **189**, 207–224 (2010).
- 316 53. Pompilio, M., Bertagnini, A., Del Carlo, P. & Di Roberto, A. Magma dynamics within a  
317 basaltic conduit revealed by textural and compositional features of erupted ash: The December 2015  
318 Mt. Etna paroxysms. *Sci. Rep.* **7**, 1–14 (2017).
- 319 54. Suzuki, Y. & Fujii, T. Effect of syneruptive decompression path on shifting intensity in basaltic  
320 sub-Plinian eruption: Implication of microlites in Yufune-2 scoria from Fuji volcano, Japan. *J.*  
321 *Volcanol. Geotherm. Res.* **198**, 158–176 (2010).
- 322 55. Wall, K. T., Rowe, M. C., Ellis, B. S., Schmidt, M. E. & Eccles, J. D. Determining volcanic  
323 eruption styles on Earth and Mars from crystallinity measurements. *Nat. Commun.* **5**, 1–8 (2014).
- 324 56. Cannata, C. B. *et al.* First 3D imaging characterization of Pele’s hair from Kilauea volcano  
325 (Hawaii). *Sci. Rep.* **9**, 1–13 (2019).
- 326 57. Holt, S. J. *et al.* Eruption and fountaining dynamics of selected 1985–1986 high fountaining  
327 episodes at Kīlauea volcano, Hawai’i, from quantitative vesicle microtexture analysis. *J. Volcanol.*  
328 *Geotherm. Res.* **369**, 21–34 (2019).
- 329 58. Lormand, C. . *et al.* Slow ascent of unusually hot intermediate magmas triggering Strombolian  
330 to Plinian eruptions. *J. Petrol.* (2020) doi:10.1093/petrology/egaa077.

331 59. Gardner, J. E., Llewellyn, E. W., Watkins, J. M. & Befus, K. S. Formation of obsidian  
332 pyroclasts by sintering of ash particles in the volcanic conduit. *Earth Planet. Sci. Lett.* **459**, 252–263  
333 (2017).

334 60. Tuffen, H., Dingwell, D. B. & Pinkerton, H. Repeated fracture and healing of silicic magma  
335 generate flow banding and earthquakes? *Geology* **31**, 1089–1092 (2003).

## 336 **Acknowledgments**

337 Manuela Nazzari provided essential support during the FESEM analyses. Partial financial support from  
338 INGV (project UNO) to JT, Deutsche Forschungsgemeinschaft project CI 254/2-1 to CC, and DGAPA-  
339 UNAM to HDG is acknowledged. B. Zimanowski, R. Büttner and I. Sonder are acknowledged for the  
340 fragmentation experiments.

341 **Author contributions.** JT conceptualized this study, contributed to sample collection and  
342 fragmentation experiments, and performed the majority of FESEM analyses. CC, MAAI, and HDG  
343 contributed to conceptualize the study and to sample collection and FESEM analyses. DA, PS, EDB,  
344 and FDS contributed to sample collection and FESEM analyses. All authors wrote the manuscript  
345 together.

346 **Competing interests.** The authors declare no competing interest.

347 **Materials & Correspondence.** Correspondence and material requests should be addressed to Jacopo  
348 Taddeucci (email: jacopo.taddeucci@ingv.it).

## 349 **Figure Captions**

350 **Fig. 1:** Scanning electron micrographs of broken crystals and healing fractures in volcanic particles  
351 from different eruptions. a-f): Crystals with increasing density and complexity of melt-filled fractures,



352 from single fractures to shattered crystals. g-k): Crystals with increasingly open fractures, from  
353 fractures with small vesicles to largely open, multiple fractures. l-o): Melt- and crystal-breaking  
354 fractures with increasing degrees of healing, from fractures with sharp boundaries (l), through partly  
355 healed fractures surrounded by viscously deformed melt (m,n), to completely healed fractures leaving a  
356 trail of broken crystals, small vesicles, and Fe-rich glass wisps (o). Grey tones from black to white are:  
357 voids (vesicles, fractures, and grain boundaries); plagioclase; glass; pyroxene and olivine and Fe- and  
358 Mg-rich glass; and Fe- Ti-oxides. Full-scale images are provided in Supplementary Data 1 and 2.

359 **Fig. 2:** Fracturing of basaltic melt during fragmentation experiments. a-d): High-speed video frames  
360 showing fracture initiation (red arrows) and propagation through the top of the basaltic melt within the  
361 cylindrical crucible (see Supplementary Video 1). e): Photograph of the upper surface of an  
362 experimental product. Fractures through the upper surface show the partially crystallized, vesicular,  
363 glassy interior of the specimen, which also includes fractured crystals. f): Polarised light micrograph of  
364 the cross-section of the specimen in (e). One of the fractures cuts through the more crystal-rich upper  
365 part of the basalt into the glass-rich interior.

366 **Fig. 3:** Scanning electron micrographs of the experimental products and broken crystals and healing  
367 fractures therein. a): A large fracture propagating downwards from the sample surface (same as Fig.  
368 2f). Viscous deformation of the melt around the lower part of the fracture locally forms isolated  
369 vesicles (red arrows). Red letters mark the location of other panels. b-e): Large, partly healed fractures  
370 are surrounded by broken crystals that record the passage of multiple, narrow fractures now completely  
371 healed (red box in (d) is magnified in (e)). f): The partially crystallized, homogeneous sample interior  
372 from another experiment, with vesicle chains formed by the passage and healing of fractures, as  
373 witnessed by the broken crystals surrounding them (g-j). k-m): Broken crystals in ash-sized

374 experimental products, with Fe-rich sutures from healed fractures. Comparative tables of natural and  
375 experimental products are provided in Supplementary Data 1.

376 **Fig. 4:** Parameters of fractures in broken crystals from eruptions and experiments. Length, width,  
377 aspect ratio, and tortuosity of fractures in natural (a,c) and experimental (b,d) products, for different  
378 fracture and crystal types. a,b): in colour, fracture tortuosity (the ratio of fracture length to the straight  
379 distance between its extremities). Note logarithmic colour scale. Red lines and numbers represent  
380 constant values of aspect ratio (the ratio of fracture length to its width). Length and width measurement  
381 error, estimated by repeated measurements, is  $< 13\%$  of the given value. c,d): Statistical values for the  
382 parameters. The top and bottom of boxes are the 25th and 75th percentiles of the samples, respectively,  
383 while the middle of each box is the sample median. Whiskers span 1.5 times the interquartile range.

384 **Fig. 5:** Proposed processes involved in the fragmentation of a parcel of basaltic magma rising along the  
385 conduit of an erupting volcano. Colours indicate silicate melt (red), gas bubbles (white), silicic (blue)  
386 and mafic (yellow) crystals, and fractures (black). During magma ascent (a), exsolved gas pockets  
387 expand rapidly and accelerate the magma until rapid deformation and stress accumulation induces  
388 brittle fracturing (b). Large fractures propagate through the magma and isolate individual pyroclasts.  
389 Narrower fractures are healed by viscous deformation of the melt, leaving additional bubbles and  
390 broken crystals in the pyroclasts (c).

## 391 **Methods**

### 392 **Eruption case studies background and sampling information**

393 We found broken crystals within pyroclasts of the following eruptions and styles: Etna (Italy) 2001 and  
394 2002-2003 flank eruptions<sup>62,63</sup>; Parícutin (Mexico) 1943, Xitle (Mexico) 2 ka, and Croscat (Spain) 11  
395 ka violent Strombolian eruptions<sup>64–66</sup>; Eyjafjallajökull (Iceland) 2010 complex eruption<sup>67</sup>; Fuego

396 (Guatemala) 2012 and Stromboli (Italy) July 2019 and August 2019 paroxysmal eruptions<sup>68–70</sup>; and  
397 Stromboli (Italy) 2019 persistent, normal Strombolian activity<sup>71</sup>. These cases include eruptions with  
398 and without accompanying lava effusion, eruption plumes and ejecta height from few hundred metres  
399 to few kilometres, magma ascent rates from 0.1 to 30 m s<sup>-1</sup>, magma discharge rates from 10<sup>2</sup> to 10<sup>6</sup> kg  
400 s<sup>-1</sup>, continuous ejection duration from few seconds to few days, and whole eruption duration from few  
401 months to centuries<sup>27,69,72–74</sup>. Whole rock composition of the erupted magmas ranges from basanite,  
402 through basalt, trachybasalt and basaltic andesite, to andesite (SiO<sub>2</sub> range 44 to 60 wt.%)<sup>63,65–68,75–79</sup>,  
403 while interstitial glass compositions, representative of the melt in between the crystals, range from  
404 basanite, through basalt, basaltic andesite, andesite and benmoreite, to trachyte and dacite (SiO<sub>2</sub> range  
405 44 to 65 wt.%)<sup>34,61,78–81</sup>. All products include microlite- to microphenocrystal-sized crystals of  
406 plagioclase, pyroxene, olivine, and Fe- and Ti-oxides, in a groundmass that can be either glassy or  
407 microcrystalline. Domains of the two types of groundmass are often found intermingled within the  
408 same pyroclasts, as visible in Extended Data Fig. 2 and Supplemental Data 2. Extended Data Table 1  
409 reports the crystallinity of some of the erupted products.

410 Sampling information is as follows:

411 Croscat volcano (Spain), 11 ka eruption: Lapilli-sized pyroclasts were sampled from the tephra fallout  
412 deposit outcropping in the Pacte del Quesito location, as described by Di Traglia and co-authors  
413 (sections #26, 27, 55, Figs. 2, 3 and 4)<sup>65</sup>.

414 Parícutin volcano (Mexico), 1943 eruption: Lapilli-sized pyroclasts were sampled from the tephra  
415 fallout deposit in a ~3 m deep excavation we dug at coordinates N 19° 29' 55" and W 102° 15' 44"  
416 (approximately coincident with Site A as reported by Pioli and co-authors<sup>77</sup>).

417 Xitle volcano (Mexico), 2 ka eruption: Lapilli-sized pyroclasts were sampled from the tephra fallout  
418 deposit outcropping at coordinates N 19° 13' 47" and W 99° 14' 30" and N 19° 14' 27" and W 99° 13'  
419 18".

420 Etna (Italy), 2001 eruption: Volcanic ash was sampled on 26 and 29 July 2001, near the Mascalucia  
421 village (N 37° 34' 36'', E 15° 02' 58''). The samples include ash particles in the size range 100 to 400  
422 µm, collected over a time interval of 24 hours on a clean surface while settling from the eruption  
423 plume<sup>34,62</sup>.

424 Etna (Italy), 2002-03 eruption: Volcanic ash was sampled on 7 and 11 November 2002 near the Ballo  
425 locality village (N 37° 42' 17'', E 15° 06' 56'') and at the INGV building inside Catania city (N 37°  
426 30' 49'', E 15° 04' 55''), respectively. Both samples include ash particles collected over a time interval  
427 of several hours on a clean surface while settling from the eruption plume<sup>80</sup>.

428 Eyjafjallajökull, (Iceland), 2010 eruption: Volcanic ash was sampled on 19 May 2010 at coordinates N  
429 63° 42' 39'', W 19° 44' 00''. Ash particles were collected over a time interval of five hours on a clean  
430 surface while settling from the eruption plume.

431 Fuego (Guatemala), paroxysmal Strombolian activity: Volcanic ash was sampled on 13 September  
432 2012 at coordinates N 14° 26' 02'', W 90° 55' 31''. Ash particles were collected over an unknown  
433 time interval on a clean surface while settling from the 3000 m-high eruption plume of a single  
434 explosion.

435 Stromboli (Italy), 3 July 2019 paroxysmal explosion: multiple decimetre-sized volcanic bombs were  
436 sampled from the ground on 28 July 2019 at coordinates N 38° 47' 36'', E 15° 13' 00''.

437 Stromboli (Italy), 28 August 2019 paroxysmal explosion: multiple decimetre-sized volcanic bombs  
438 were sampled from the ground on 7 September 2019 at coordinates N 38° 47' 33'', E 15° 12' 50''.

439 Stromboli (Italy), ongoing Strombolian activity: Volcanic ash was sampled on 11 May 2019 at  
440 coordinates N 38° 47' 45'', E 15° 12' 59''. Ash particles were collected over a time interval of a few  
441 minutes on a clean surface while settling from the eruption plumes of individual explosions from  
442 different vents.

#### 443 **Imaging and measurements**

444 Microscopic observations were performed using a JEOL 6500 Field Emission Scanning Electron  
445 Microscope (FESEM), operated at accelerating voltage between 15 and 20 kV and variable emission  
446 current, and using Back-Scattered electrons as imaging source. The Etna samples were observed using  
447 a Cambridge Stereoscan 360 Scanning Electron Microscope. In total, more than 3 bomb-sized, 60  
448 lapilli-sized, and 300 ash-sized pyroclasts were investigated in detail at magnifications between 10 and  
449 100,000 x, for a total of more than 650 hours of observation. Extensive visual documentation of the  
450 natural and experimental products is available in the Supplementary Information files.

451 The groundmass crystallinity of selected samples and of the experimental products was measured on  
452 FESEM images at magnifications between 180 and 350 x, by both image segmentation and point  
453 counting methods, counting a minimum of 500 randomly distributed points for each image. The results  
454 of the two methods are congruent within ~10%. Crystallinity was measured in pyroclasts with a glassy  
455 groundmass only, and all values in Extended Data Table 1 are provided on a vesicle-free basis.

456 Quantitative crystal fracture parameters were measured from the FESEM images. The fractures were  
457 parameterised by measuring their bi-dimensional length, mean width, aspect ratio, and tortuosity. The  
458 aspect ratio is calculated as the ratio of the fracture length to its mean width, and tortuosity as the ratio  
459 of the length of the fracture to the straight distance between its extremities. 325 fractures were  
460 measured in the products of the different eruptions, and 307 in the products of the different  
461 experiments.

462 The bi-dimensional fracture number density was obtained from the total number of crystal fragments  
463 per unit area of the particle (on a vesicle-free basis), and, based on the observation of the micrographs  
464 in Supplementary Information S1, assuming that each fragment is bounded on average by two  
465 fractures. The obtained numbers are lower bounds, because the occurrence of finely fragmented  
466 crystals (e.g., Fig. 1f) produces locally much higher fracture number densities at the micrometric scale.

## 467 **Fragmentation experiments**

468 Fragmentation experiments were performed following Büttner and co-authors<sup>33</sup>. The selected starting  
469 material was lapilli-size pyroclasts from the explosive activity that took place at 2700 m elevation on  
470 the southern flank of Mt. Etna during the 2002-03 eruption. The experimental set-up includes a heating  
471 system and an injection system. In the heating system, a steel crucible (inner diameter 10 cm) with  
472 removable lid contains 0.3 to 0.5 kg of granulate starting material and is surrounded by a water-cooled  
473 copper coil. Electric current from a radio-frequency generator circulates in the coil and inductively  
474 heats up the crucible that melts the rock. The injection system connects the base of the crucible to a  
475 pressurized Argon gas reservoir and a computer-controlled solenoid valve that allows impulsive  
476 injection of the gas at the base of the melt. We used a thermocouple (S-type, Pt/PtRh, temperature  
477 range 50 – 1750 °C, tolerance 0.5%) to measure temperature at the surface of the melt. During  
478 preliminary test runs we defined the best heating path to obtain a melt that would represent at best the  
479 range of crystal abundance and size of the natural products. All runs started with an identical heating  
480 ramp that reached 1275 °C in 100 minutes, a dwell at the same temperature for 90 minutes during  
481 which the sample melted completely, and a cooling ramp to 1160 °C in 30 minutes. This latter  
482 temperature was kept constant for a time interval that varied from 90 to 180 minutes in the different  
483 runs, resulting in a variable melt crystallization. Final run procedures included hand-stirring to  
484 homogenize the melt about 10 minutes before the injection, cooling to the final temperature of 1080 °C

485 in 5-10 minutes, removal of crucible lid, and gas injection for a duration of 0.03s. Gas injection  
486 fragments the sample and ejects it out of the melt. A total of 17 experiments were performed, including  
487 test and repeated runs, to obtain the 11 experiments with different degree of melt crystallinity reported  
488 in Extended Data Table 1. Sample fragmentation was recorded using a NAC HotShot 512 high speed  
489 camera recording at 5000 frames per second and 512x512 pixel resolution.

490 Petrographic micrographs and FESEM analyses reveal that in all experimental products the top few  
491 microns of the sample display an entirely crystallized crust of sub-micron sized crystals. The rest of the  
492 sample displays a range of crystallinity features function of the duration of the crystallization interval.  
493 Features include relic phenocrysts, skeletal aggregates of plagioclase and pyroxenes, and microlites of  
494 plagioclase, pyroxene, olivine and oxides. Total crystal content ranges from 3 to 63 vol. % (Extended  
495 Data Table 1). Melt viscosity at fragmentation, calculated from the starting material composition<sup>63,80</sup>,  
496 the measured crystallinity (Extended Data Table1), the experimental temperature, and the model of  
497 Giordano and co-authors<sup>82</sup>, ranges from  $10^{2.3}$  to  $10^{4.5}$  Pa s, in line with estimated melt viscosities during  
498 the 2001 Etna eruption and with experimental measurements of Etna melt viscosity during  
499 crystallization<sup>34,83</sup>. The spatial distribution of crystals within the sample ranges from mostly  
500 homogeneous to patchy as the result of heterogeneous crystallization of the melt, experimental  
501 procedures, and melt deformation during ejection.

## 502 **Time scales**

503 The time scale for fracture propagation is constrained by our high-speed video observation to be  $<10^{-4}$  s  
504 (Fig. 2), in agreement with the measured time scale of  $10^{-7}$  s for a fracture 100  $\mu\text{m}$  long propagating in  
505 synthetic glass analogues for high-temperature basalt<sup>49</sup>. The time scale for the onset of healing after  
506 initial contact of two basaltic melt parcels can be estimated to be of the order of  $10^{-6}$  to  $10^{-5}$  s, following  
507 experimental results obtained for silicic magmas<sup>46</sup> and a constant melt viscosity in the range of  $10^2$  to

508  $10^{4.5}$  Pa for the melt composition, crystallinity, and temperature of most of our experimental and  
 509 natural cases (see above)<sup>82</sup>. An upper limit of the time scale for complete fracture healing can be  
 510 estimated considering surface tension as the only driving force and neglecting the intervention of other  
 511 forces<sup>46</sup> (e.g., local pressure gradients, magma rise and vesiculation, gas drag). For a constant melt  
 512 viscosity in the range of  $10^2$  to  $10^{4.5}$  Pa s, a surface tension at the melt-vapour interface ranging from  
 513  $0.05$  to  $0.1 \text{ N m}^{-1}$ <sup>84</sup>, and the observed range of fracture width from  $0.1$  to  $10 \text{ }\mu\text{m}$  (Fig. 4), the time for  
 514 magma flow to close the fracture ranges from  $10^{-4}$  to  $1$  s. This analysis applies to fractures in melt only,  
 515 and does not includes the flow of melt into crystals. In our conceptual model (Fig. 5), and in analogy  
 516 with more silicic cases<sup>17,85</sup>, fracturing of basaltic magma does not necessarily lead to immediate  
 517 pyroclast formation. The travel time of a fractured magma parcel before it becomes entirely separated  
 518 from the rest of the magma as a single pyroclast and is consequently accelerated by the gas phase to its  
 519 ejection velocity depends on magma ascent rate ( $10^{-1}$  to  $30 \text{ m s}^{-1}$ , see above) and fracturing depth.  
 520 Thus, this time scale ranges from zero, in the case of fracturing coincident with clast formation, to  $>10^3$   
 521 s for the slowest ascent rate and fracturing depth of the order of  $10^2$  m. The in-conduit travel time of  
 522 fractured magma as a clast before ejection depends on its rise speed in the gas-pyroclasts mixture,  
 523 which ranges from  $10$  to  $100 \text{ m s}^{-1}$ <sup>86,87</sup> for our case study eruptions, and the depth of clast formation,  
 524 assumed to be in the  $1$ - $100$  m range<sup>86</sup>, resulting in a time scale of  $10^{-2}$  to  $10$  s. The time scale required  
 525 for a clast to cool from eruptive temperature to the glass transition temperature after its ejection from  
 526 the volcanic conduit (or from the crucible, in the case of the experiments) has been calculated using the  
 527 experimentally-validated model of Moitra and co-authors<sup>41</sup>, considering the size of the investigated  
 528 clasts ( $10^{-4}$  to  $10^{-2}$  m), typical thermal conductivity for basalts of  $k = 0.6 \text{ W m}^{-1} \text{ K}^{-1}$ <sup>88</sup>, and a glass  
 529 transition temperature in between  $680$ - $650 \text{ }^\circ\text{C}$ <sup>82</sup>. Cooling after ejection of the whole clast (from the  
 530 surface to its centre) occurs in the time range from  $1$  to  $10^2$  s.

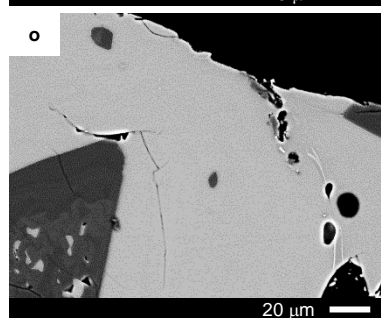
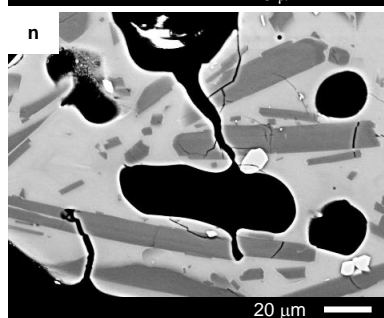
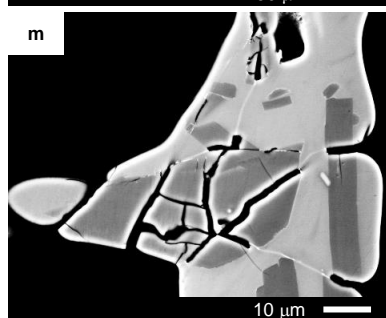
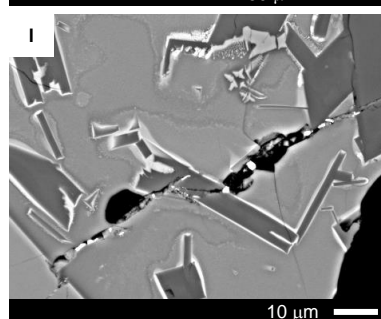
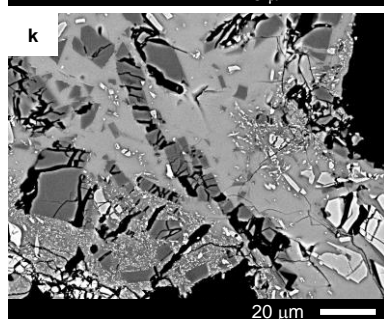
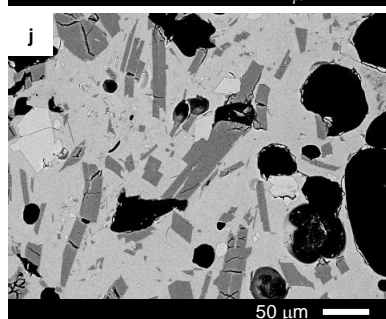
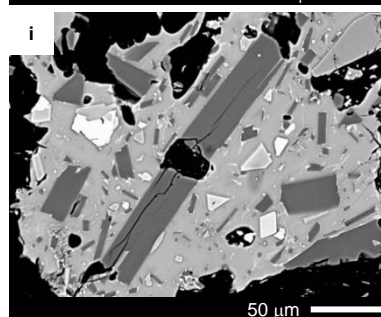
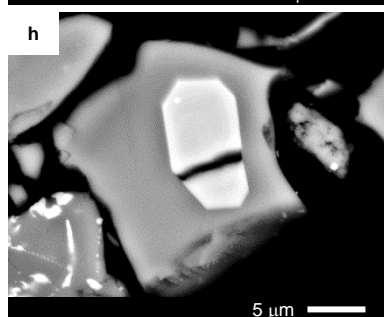
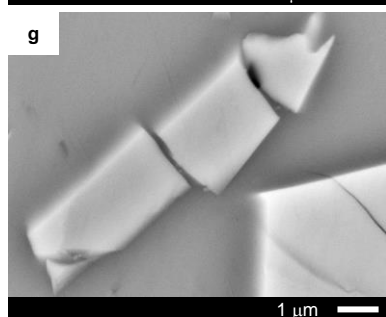
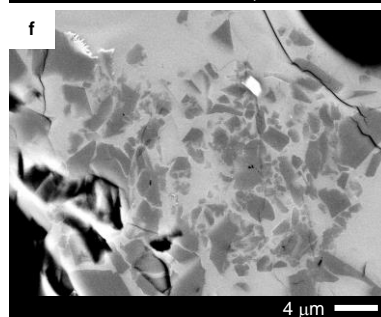
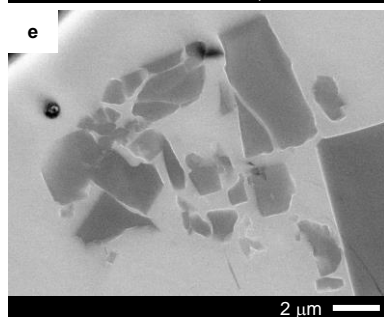
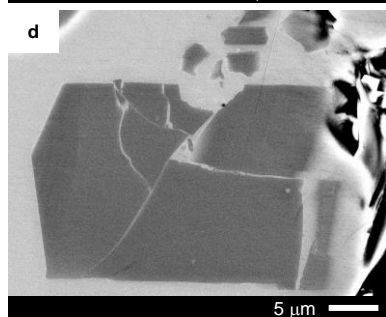
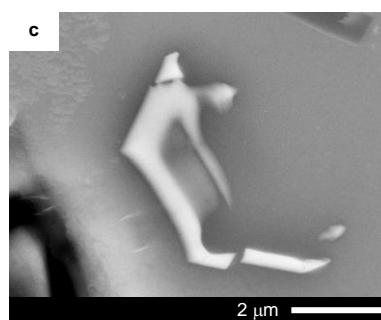
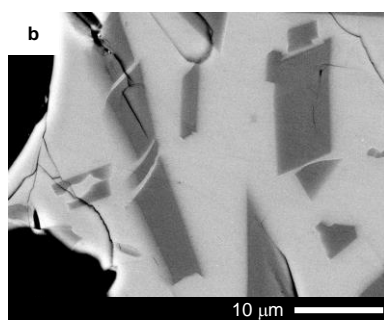
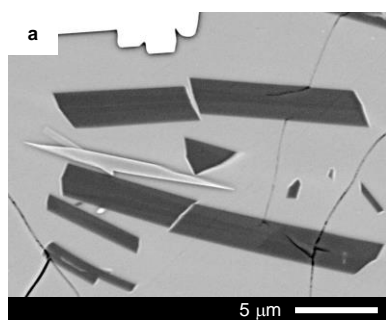
## 531 **References only in Methods**

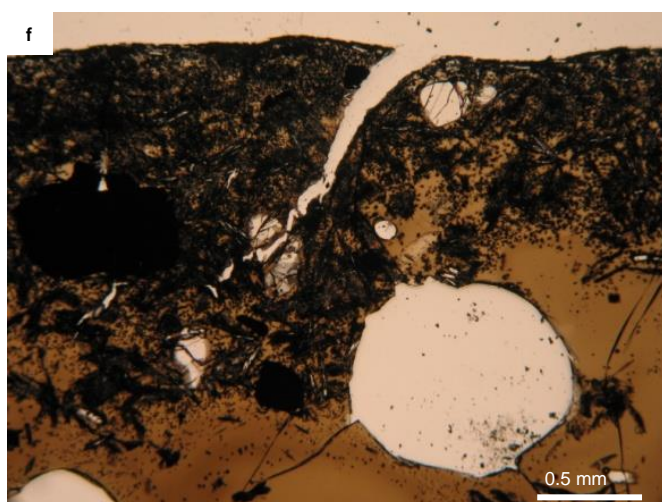
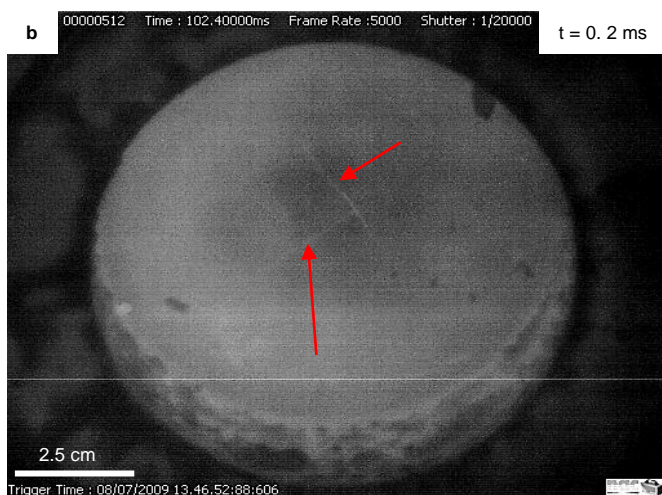


- 532 61. Cimorelli, C., Di Traglia, F. & Taddeucci, J. Basaltic scoria textures from a zoned conduit as  
533 precursors to violent Strombolian activity. *Geology* **38**, 439–442 (2010).
- 534 62. Taddeucci, J., Pompilio, M. & Scarlato, P. Monitoring the explosive activity of the July-August  
535 2001 eruption of Mt. Etna (Italy) by ash characterization. *Geophys. Res. Lett.* **29**, (2002).
- 536 63. Andronico, D. *et al.* A multi-disciplinary study of the 2002-03 Etna eruption: Insights into a  
537 complex plumbing system. *Bull. Volcanol.* **67**, 314–330 (2005).
- 538 64. Pioli, L. *et al.* The eruptive activity of 28 and 29 December 2002. *Geophys. Monogr. Ser.* **182**,  
539 105–115 (2008).
- 540 65. Di Traglia, F., Cimorelli, C., de Rita, D. & Gimeno Torrente, D. Changing eruptive styles in  
541 basaltic explosive volcanism: Examples from Croscat complex scoria cone, Garrotxa Volcanic Field  
542 (NE Iberian Peninsula). *J. Volcanol. Geotherm. Res.* **180**, 89–109 (2009).
- 543 66. Delgado, H. *et al.* Geology of Xitle volcano in southern Mexico City - A 2000-year-old  
544 monogenetic volcano in an urban area. *Rev. Mex. Ciencias Geol.* **15**, 115–131 (1998).
- 545 67. Gudmundsson, M. T. *et al.* Ash generation and distribution from the April-May 2010 eruption  
546 of Eyjafjallajökull, Iceland. *Sci. Rep.* **2**, 1–12 (2012).
- 547 68. Viccaro, M. *et al.* Shallow conduit dynamics fuel the unexpected paroxysms of Stromboli  
548 volcano during the summer 2019. *Sci. Rep.* **11**, 1–15 (2021).
- 549 69. Giordano, G. & De Astis, G. The summer 2019 basaltic Vulcanian eruptions (paroxysms) of  
550 Stromboli. *Bull. Volcanol.* **83**, 1–27 (2021).
- 551 70. Naismith, A. K. *et al.* Eruption frequency patterns through time for the current (1999–2018)  
552 activity cycle at Volcán de Fuego derived from remote sensing data: Evidence for an accelerating cycle

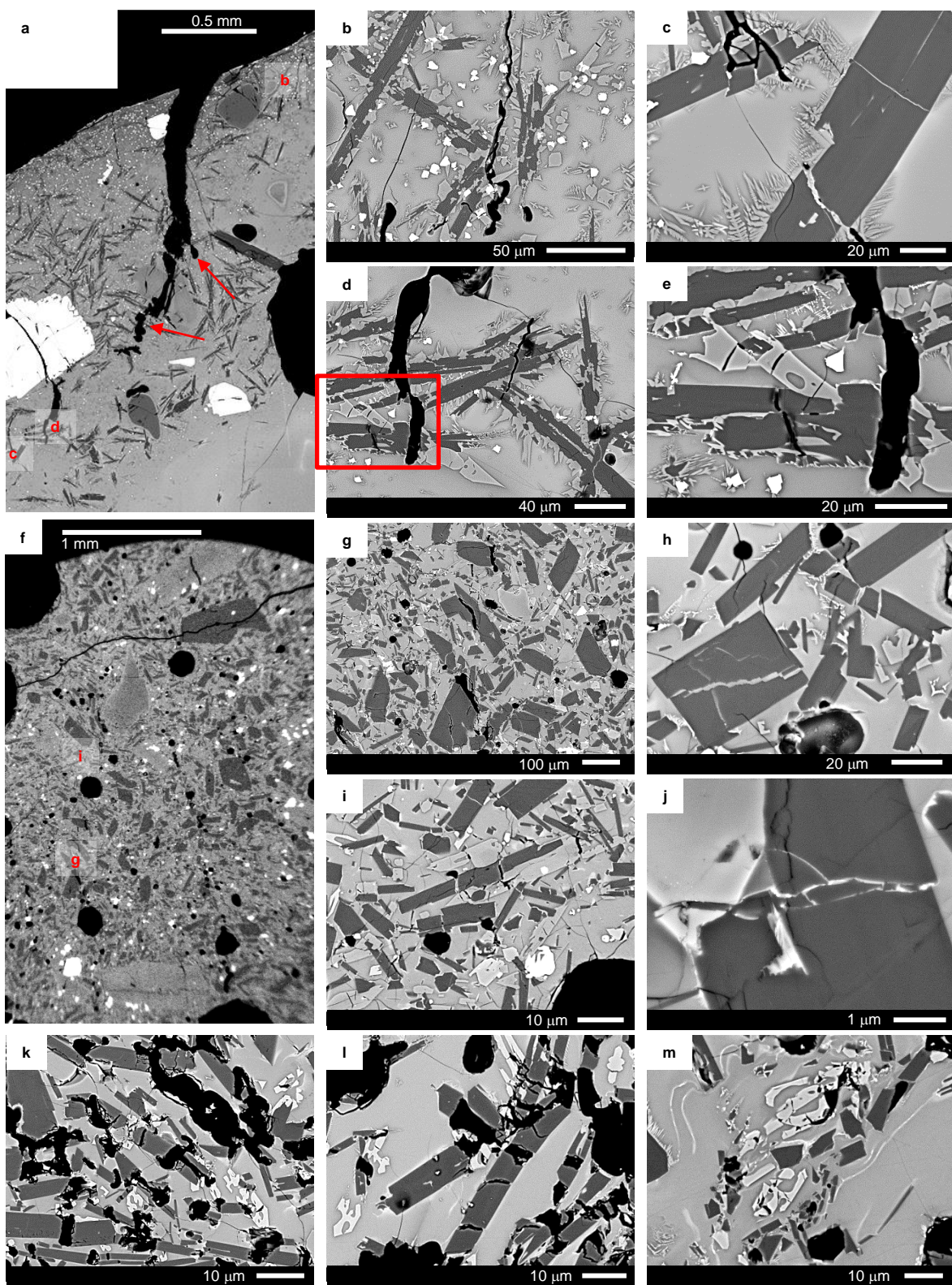
- 553 of explosive paroxysms and potential implications of eruptive activity. *J. Volcanol. Geotherm. Res.*  
554 **371**, 206–219 (2019).
- 555 71. Rosi, M. *et al.* Stromboli volcano, Aeolian Islands (Italy): Present eruptive activity and hazards.  
556 *Geol. Soc. Mem.* **37**, 473–490 (2013).
- 557 72. Lloyd, A. S. *et al.* NanoSIMS results from olivine-hosted melt embayments: Magma ascent rate  
558 during explosive basaltic eruptions. *J. Volcanol. Geotherm. Res.* **283**, 1–18 (2014).
- 559 73. Armienti, P., Perinelli, C. & Putirka, K. D. A new model to estimate deep-level magma ascent  
560 rates, with applications to Mt. Etna (Sicily, Italy). *J. Petrol.* **54**, 795–813 (2013).
- 561 74. Ripepe, M., Harris, A. J. L. & Carniel, R. Thermal, seismic and infrasonic evidences of variable  
562 degassing rates at Stromboli volcano. *J. Volcanol. Geotherm. Res.* **118**, 285–297 (2002).
- 563 75. Cervantes, P. & Wallace, P. Magma degassing and basaltic eruption styles: A case study of  
564 ~2000 year BP Xitle volcano in central Mexico. *J. Volcanol. Geotherm. Res.* **120**, 249–270 (2003).
- 565 76. Corsaro, R. A., Miraglia, L. & Pompilio, M. Petrologic evidence of a complex plumbing system  
566 feeding the July-August 2001 eruption of Mt. Etna, Sicily, Italy. *Bull. Volcanol.* **69**, 401–421 (2007).
- 567 77. Pioli, L. *et al.* Explosive dynamics of violent Strombolian eruptions: The eruption of Parícutin  
568 Volcano 1943-1952 (Mexico). *Earth Planet. Sci. Lett.* **271**, 359–368 (2008).
- 569 78. Berlo, K., Stix, J., Roggensack, K. & Ghaleb, B. A tale of two magmas, Fuego, Guatemala.  
570 *Bull. Volcanol.* **74**, 377–390 (2012).
- 571 79. Di Stefano, F. *et al.* Mush cannibalism and disruption recorded by clinopyroxene phenocrysts at  
572 Stromboli volcano: New insights from recent 2003–2017 activity. *Lithos* **360–361**, 105440 (2020).

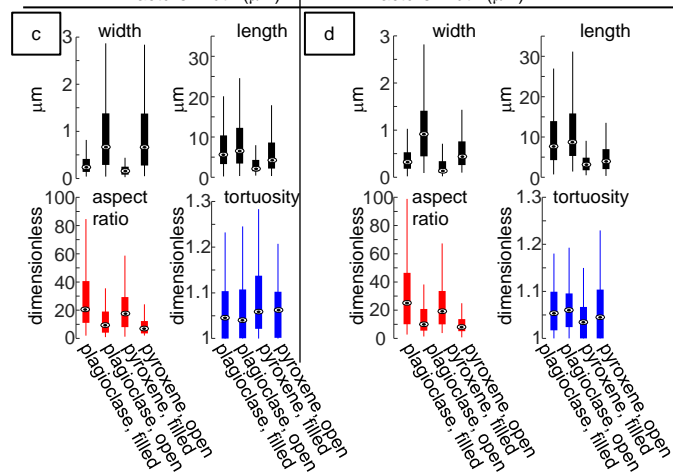
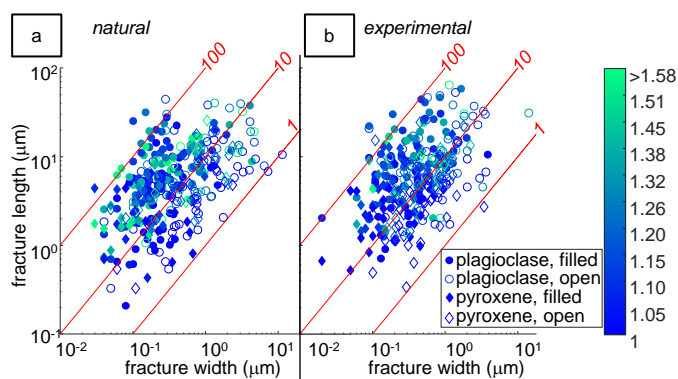
- 573 80. Andronico, D., Cristaldi, A., Del Carlo, P. & Taddeucci, J. Shifting styles of basaltic explosive  
574 activity during the 2002-03 eruption of Mt. Etna, Italy. *J. Volcanol. Geotherm. Res.* **180**, 110–122  
575 (2009).
- 576 81. Erlund, E. J. *et al.* Compositional evolution of magma from Parícutin Volcano, Mexico: The  
577 tephra record. *J. Volcanol. Geotherm. Res.* **197**, 167–187 (2010).
- 578 82. Giordano, D., Russell, J. K. & Dingwell, D. B. Viscosity of magmatic liquids: A model. *Earth*  
579 *Planet. Sci. Lett.* **271**, 123–134 (2008).
- 580 83. Vona, A., Romano, C., Dingwell, D. B. & Giordano, D. The rheology of crystal-bearing  
581 basaltic magmas from Stromboli and Etna. *Geochim. Cosmochim. Acta* **75**, 3214–3236 (2011).
- 582 84. Gardner, J. E., Ketcham, R. A. & Moore, G. Surface tension of hydrous silicate melts:  
583 Constraints on the impact of melt composition. *J. Volcanol. Geotherm. Res.* **267**, 68–74 (2013).
- 584 85. Saubin, E. *et al.* Conduit dynamics in transitional rhyolitic activity recorded by tuffisite vein  
585 textures from the 2008–2009 chaitén eruption. *Front. Earth Sci.* **4**, 59 (2016).
- 586 86. Gaudin, D. *et al.* Pyroclast Tracking Velocimetry illuminates bomb ejection and explosion  
587 dynamics at Stromboli (Italy) and Yasur (Vanuatu) volcanoes. *J. Geophys. Res. Solid Earth* **119**, 5384–  
588 5397 (2014).
- 589 87. Capponi, A., Taddeucci, J., Scarlato, P. & Palladino, D. M. Recycled ejecta modulating  
590 Strombolian explosions. *Bull. Volcanol.* **78**, 1–13 (2016).
- 591 88. Leshner, C. E. & Spera, F. J. Thermodynamic and Transport Properties of Silicate Melts and  
592 Magma. in *The Encyclopedia of Volcanoes* 113–141 (Elsevier Inc., 2015). doi:10.1016/b978-0-12-  
593 385938-9.00005-5.

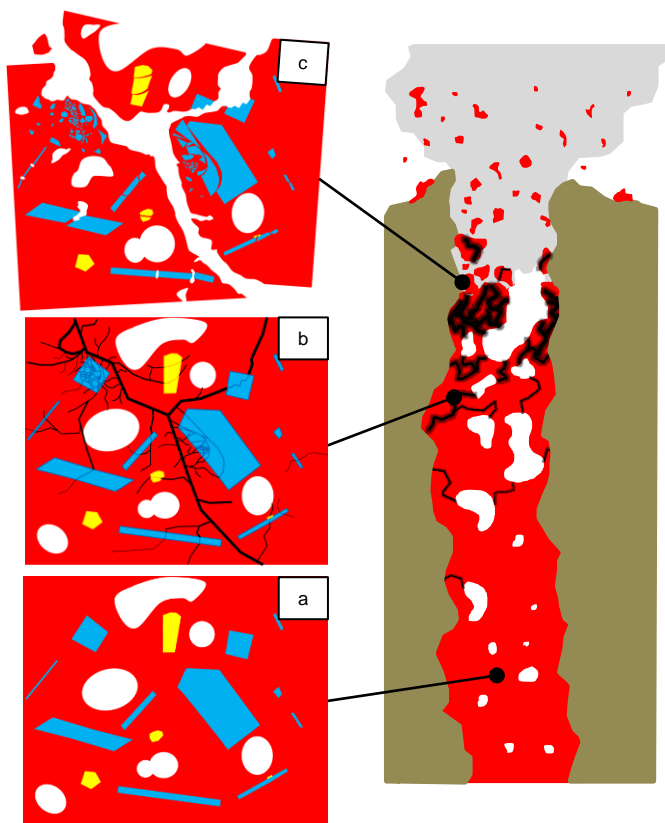












scale of microns to tens of microns

scale of metres to tens of metres



a

40-50  
2000-3000

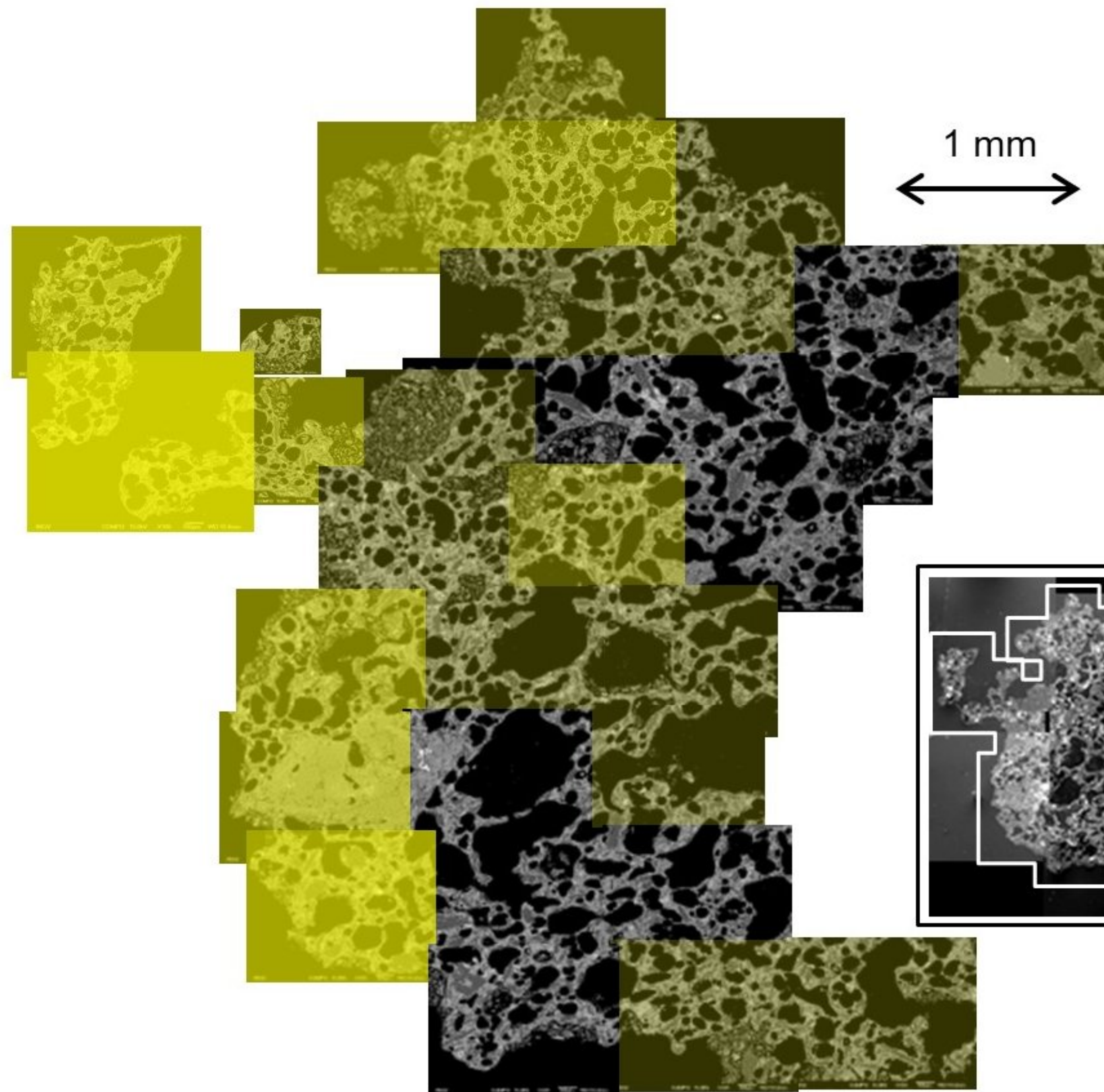
30-40  
1500-2000

20-30  
1000-1500

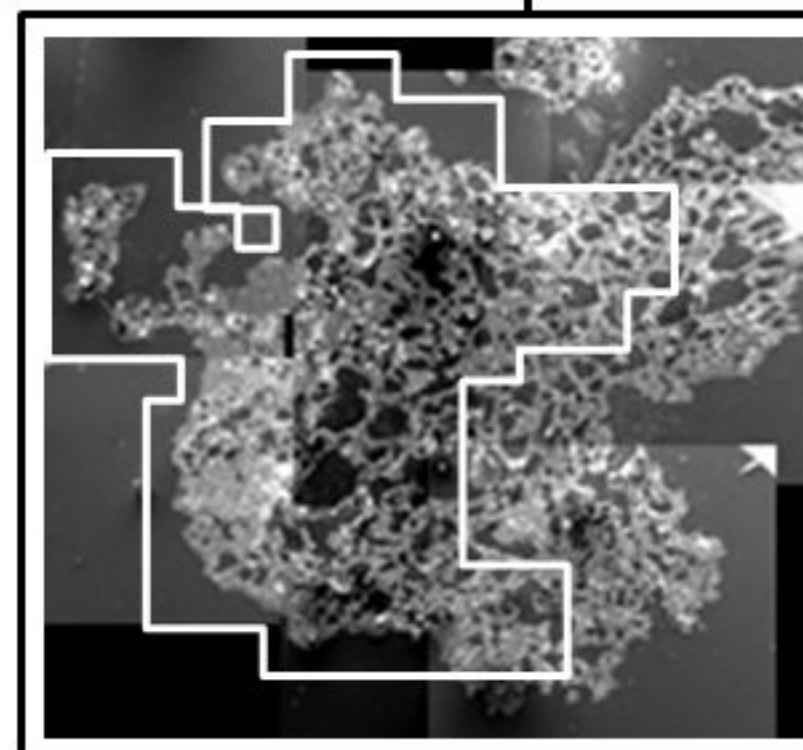
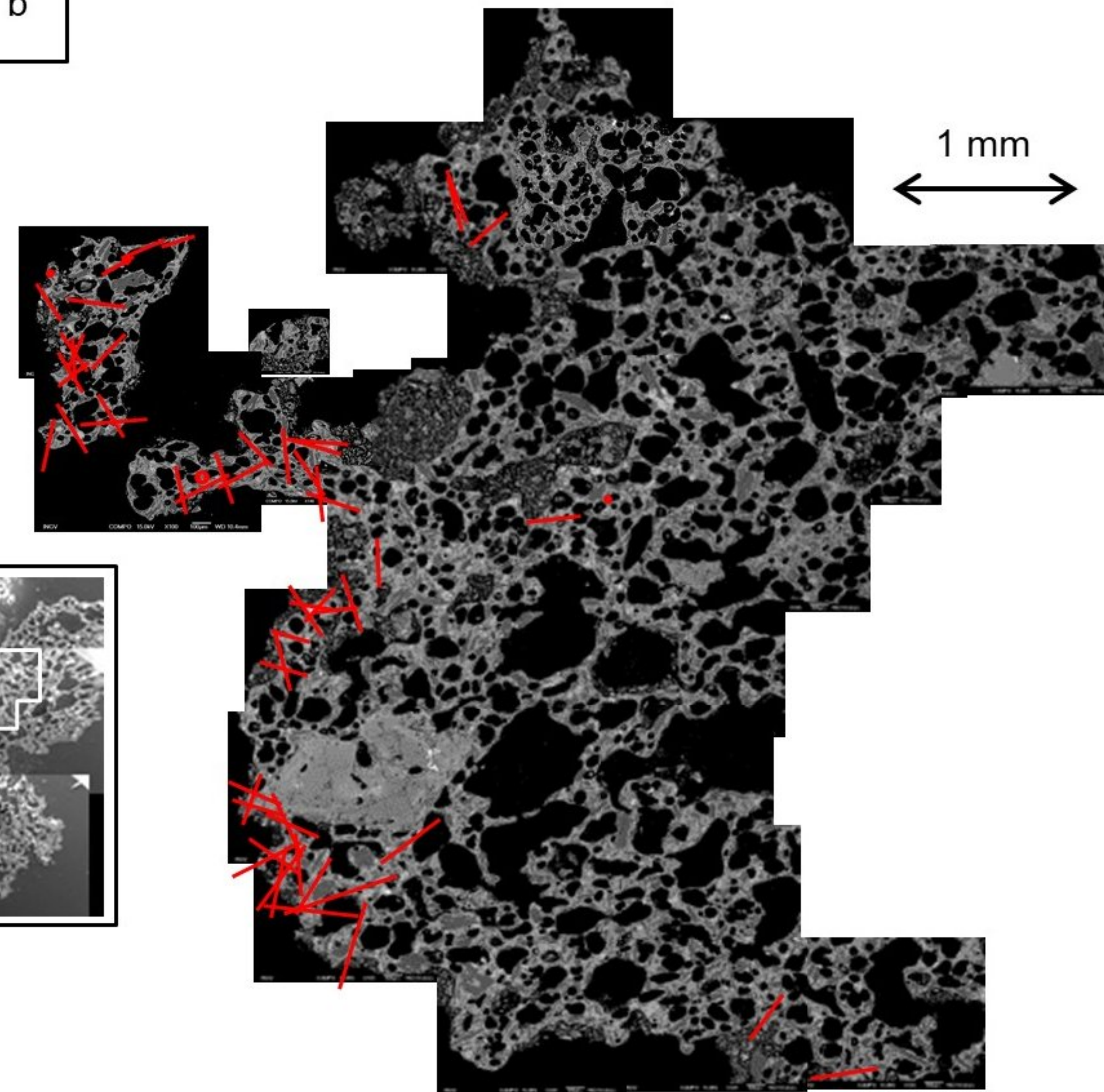
10-20  
300-1000

1-10  
0-300

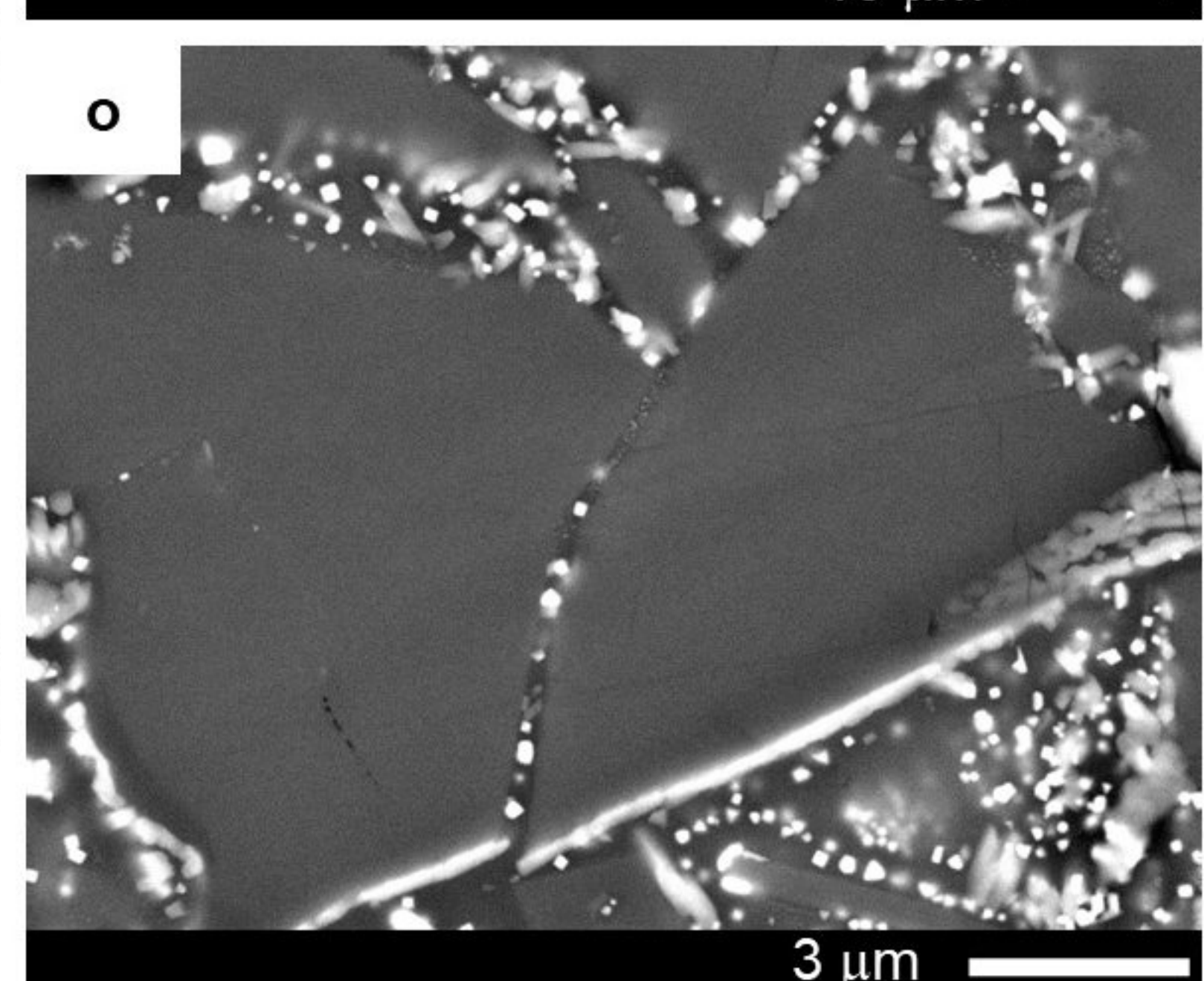
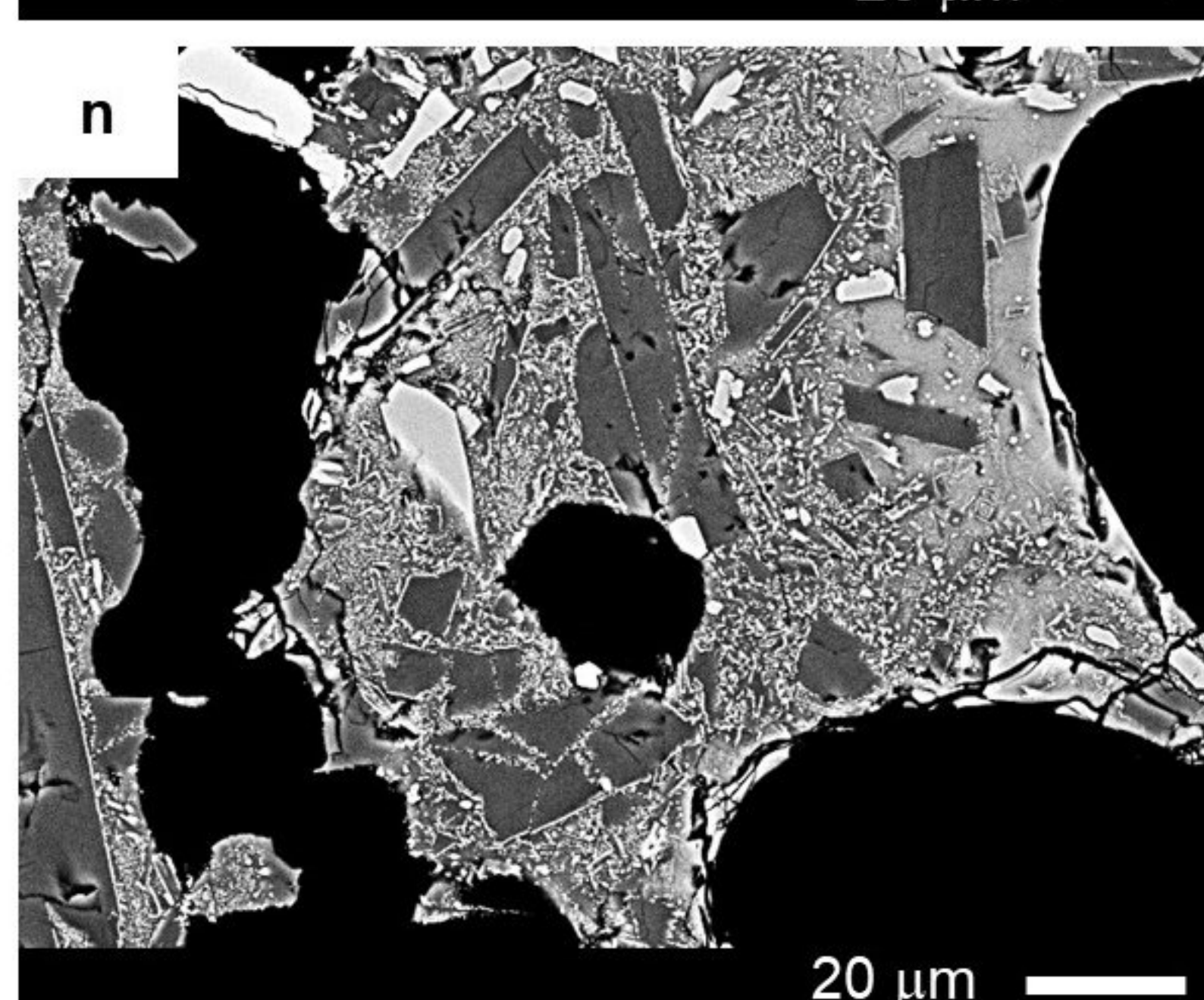
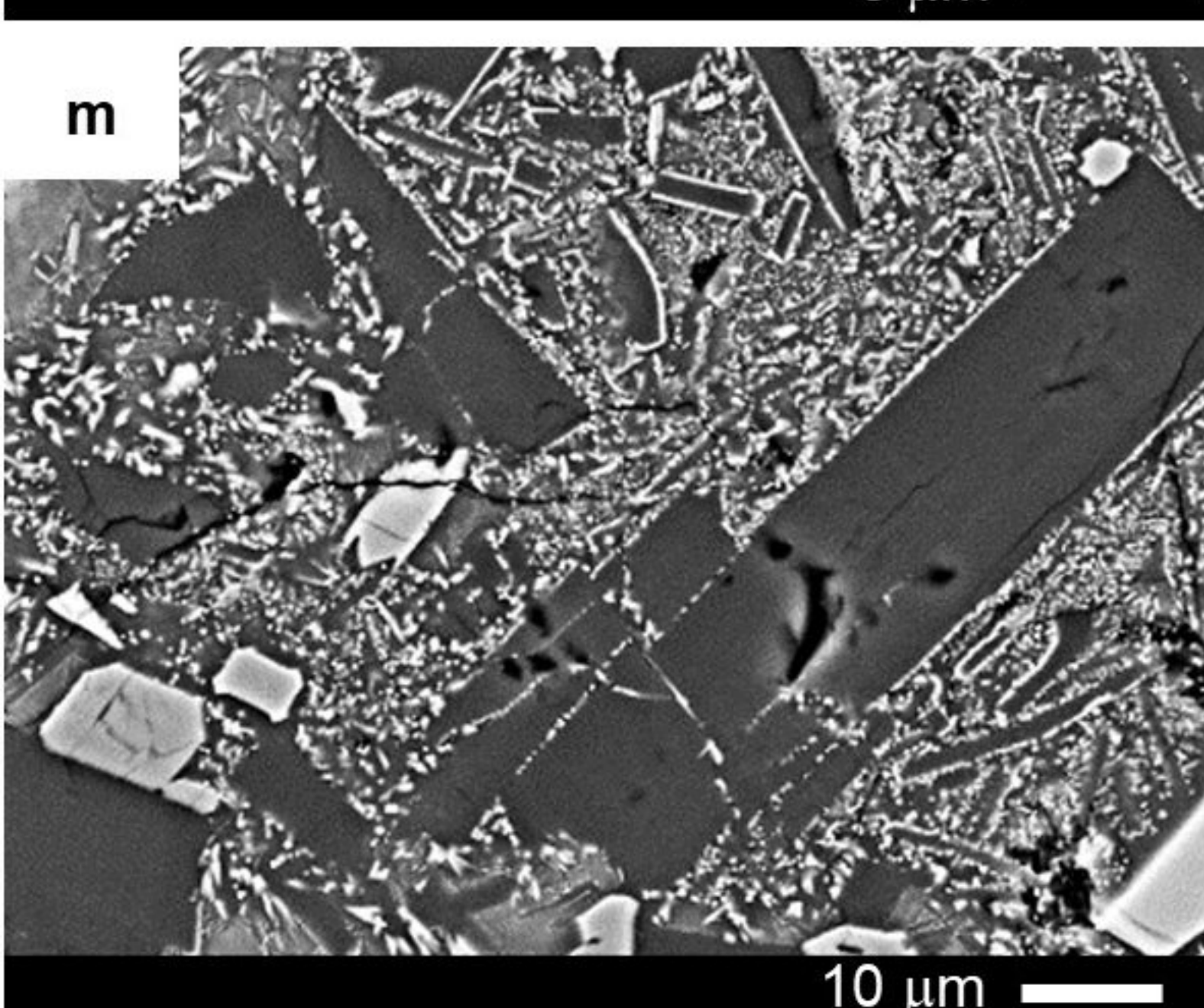
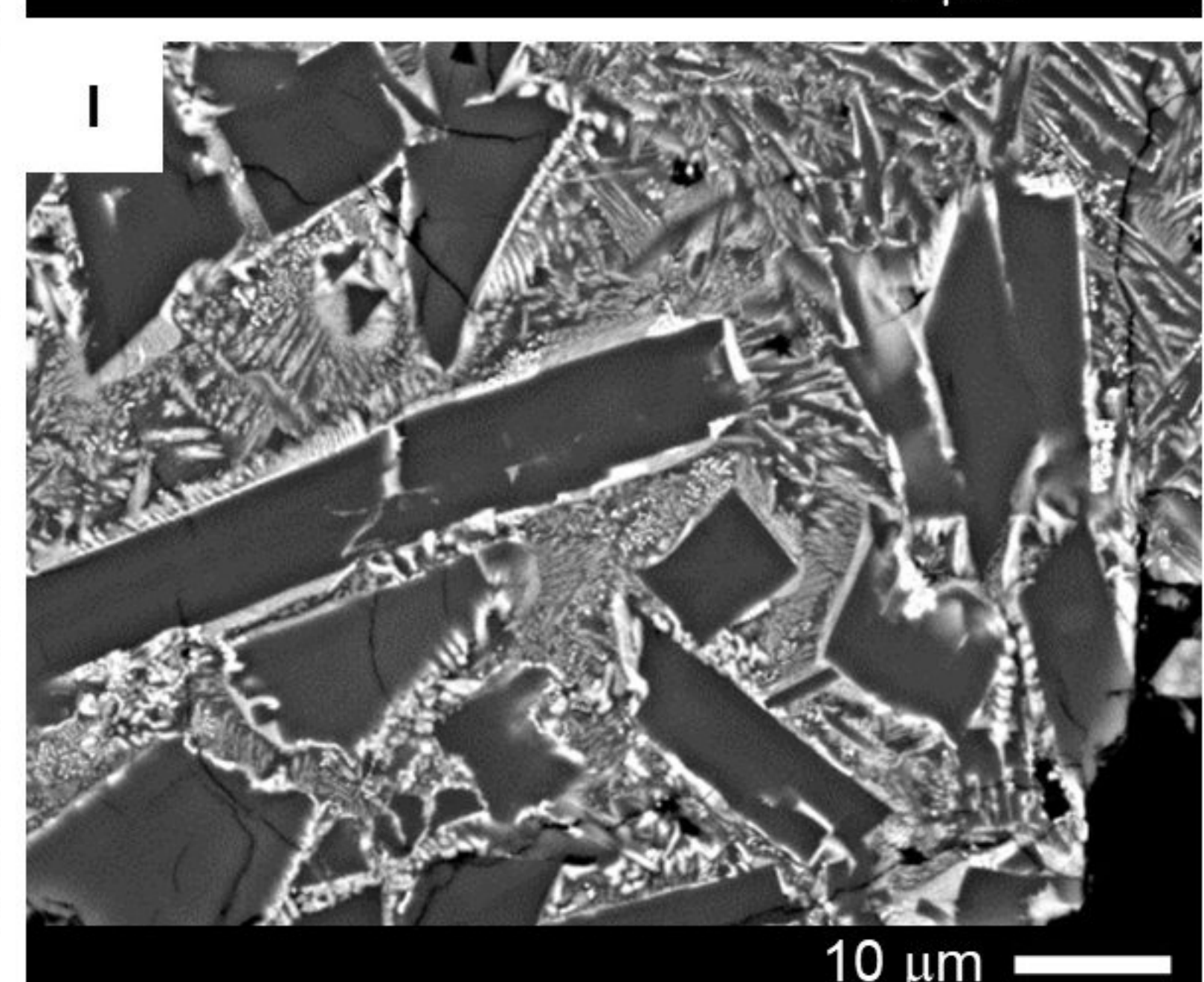
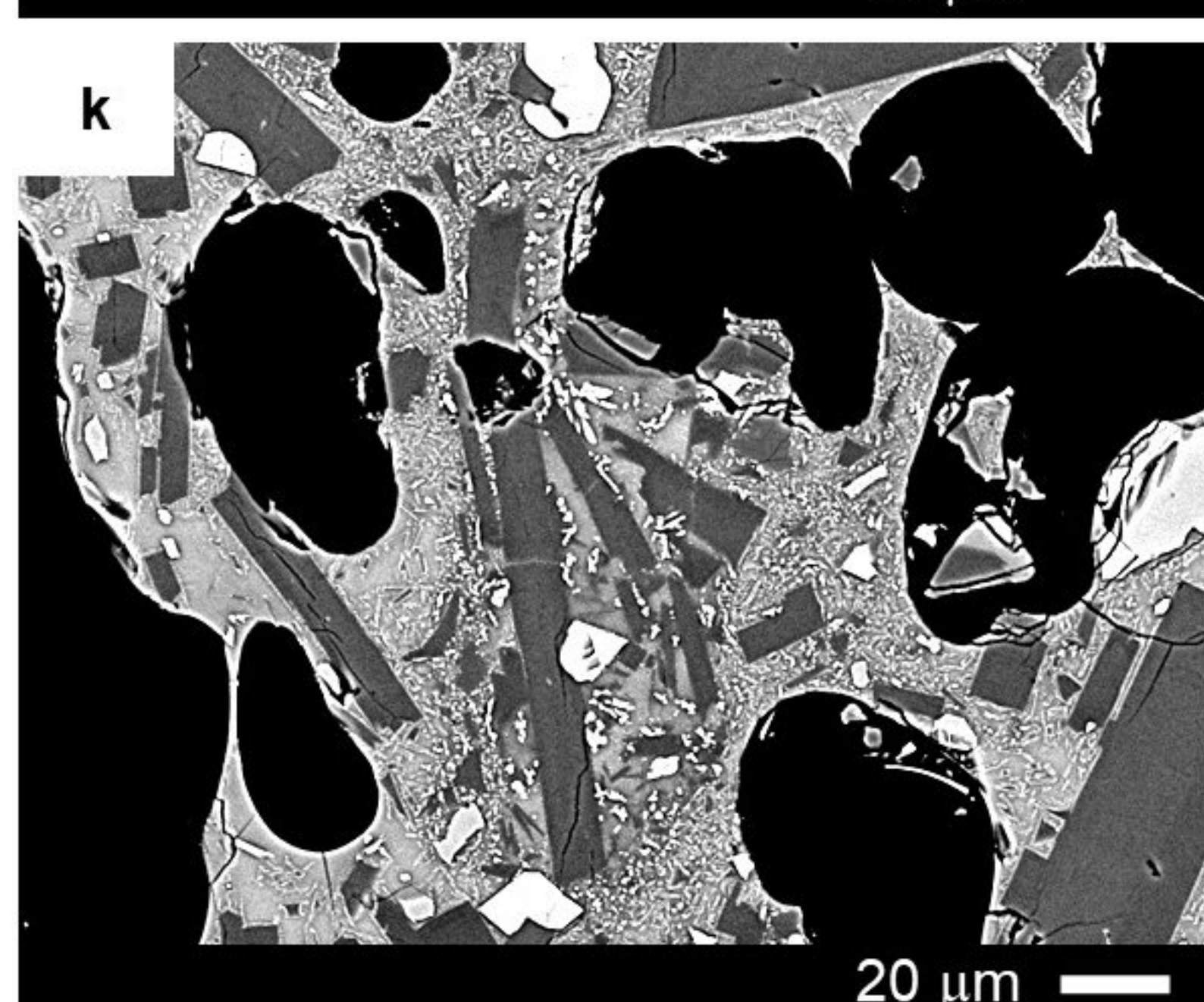
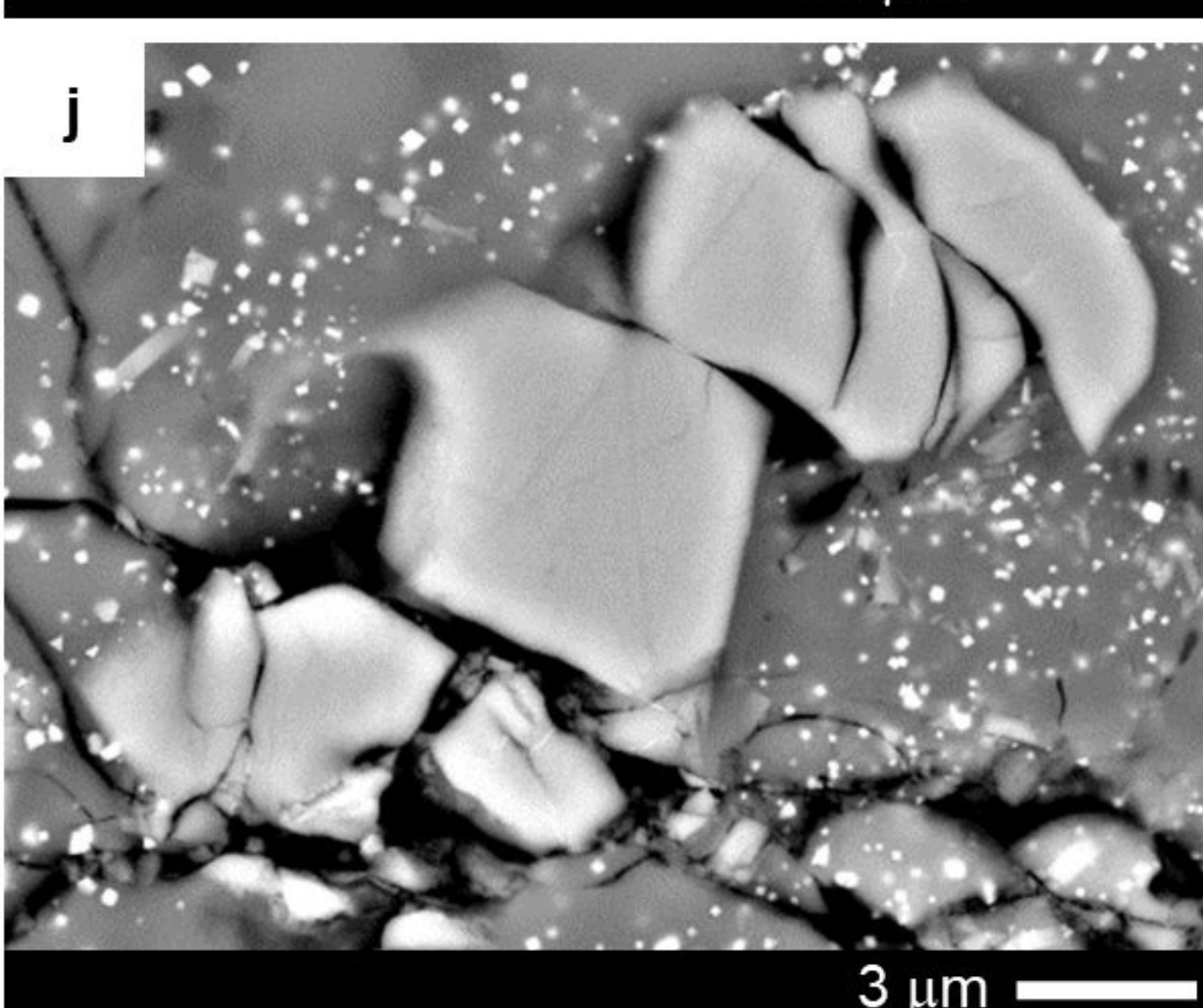
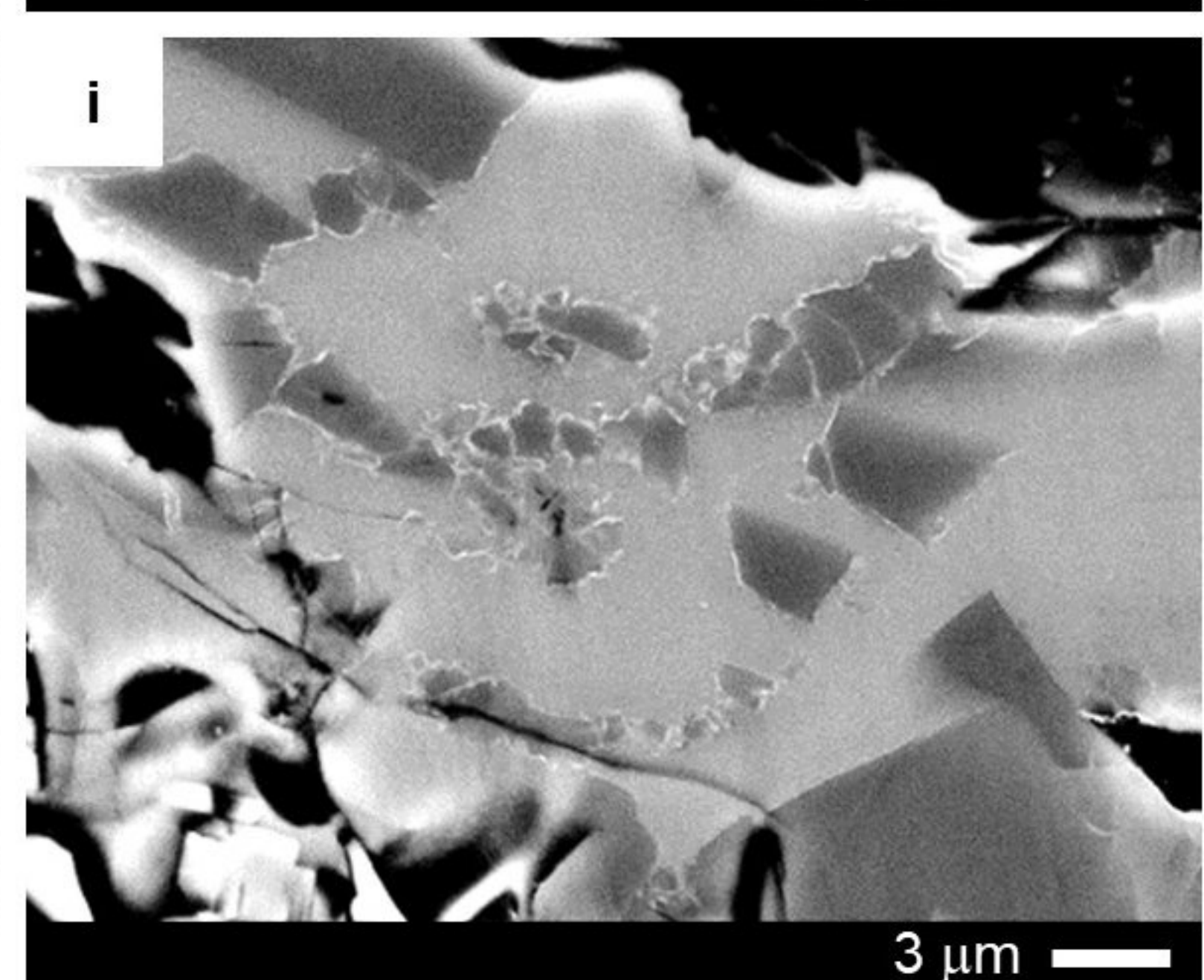
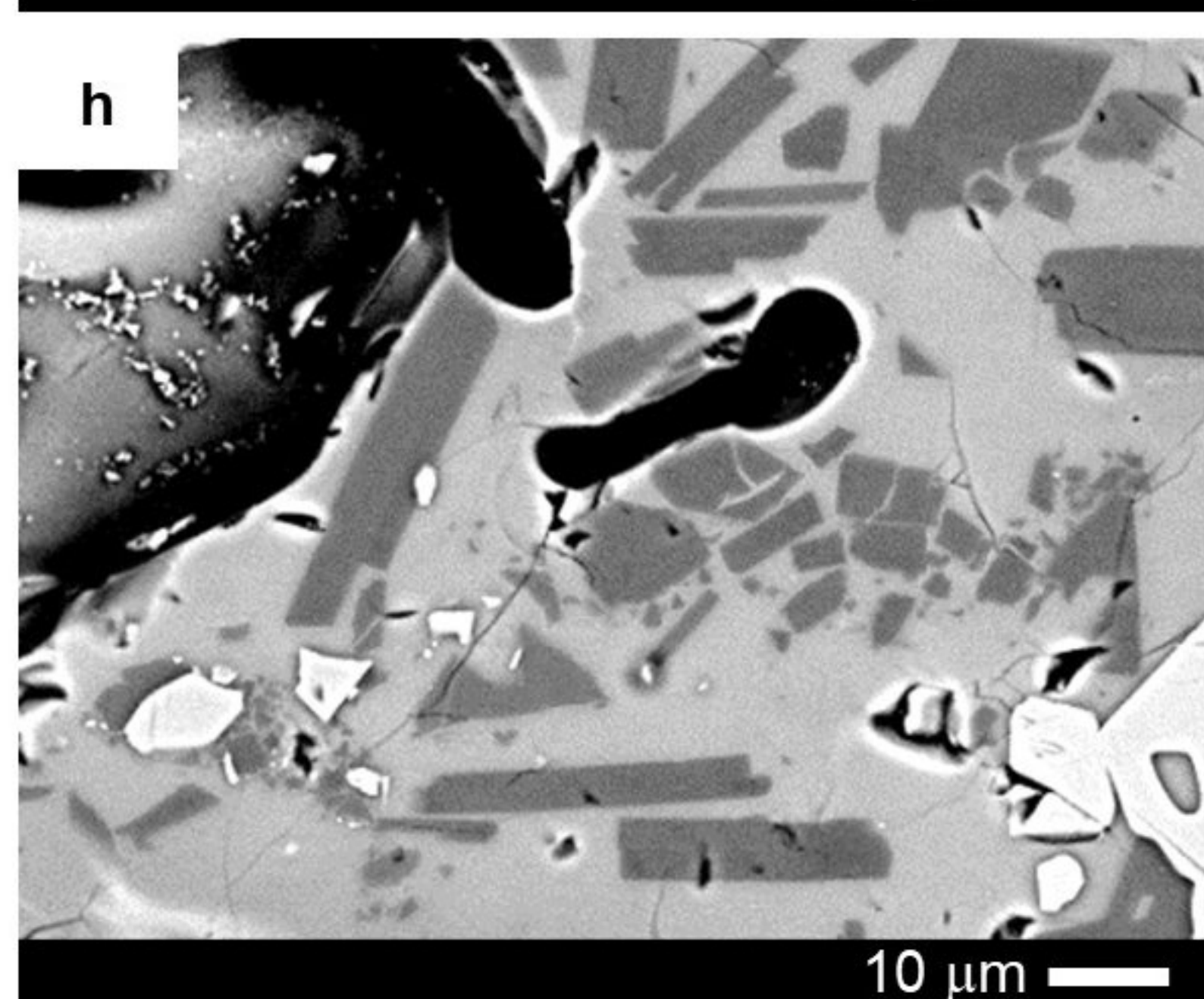
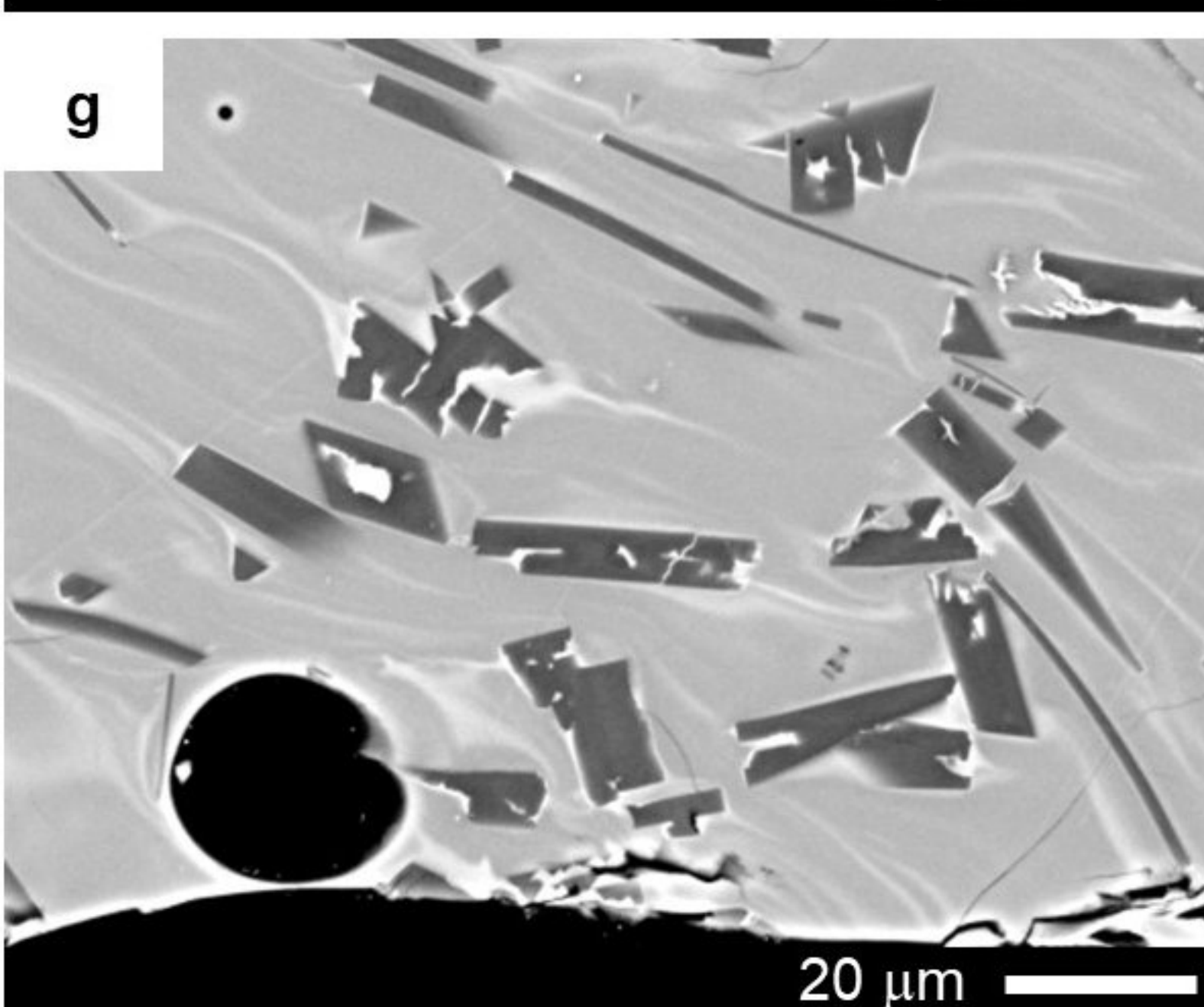
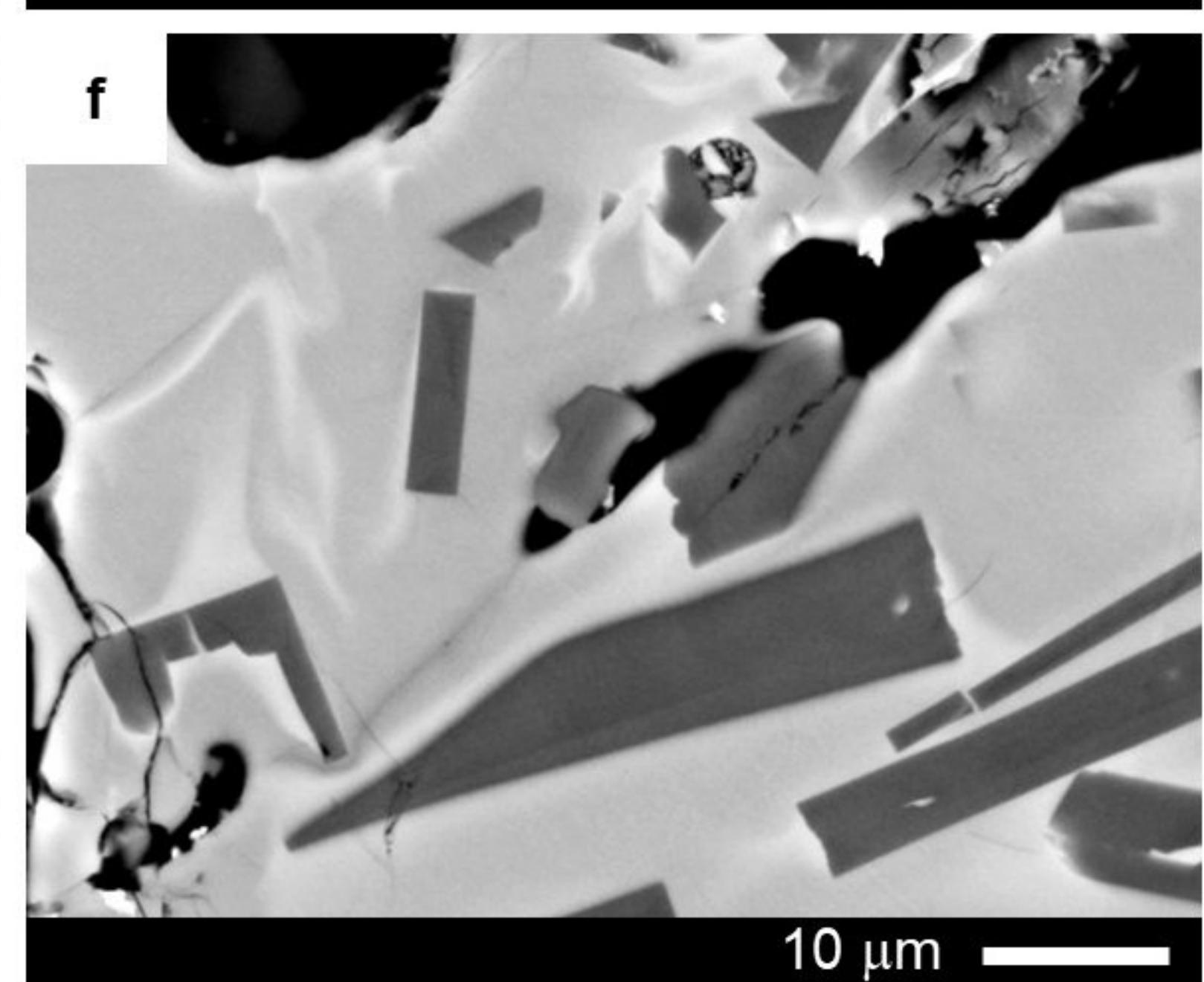
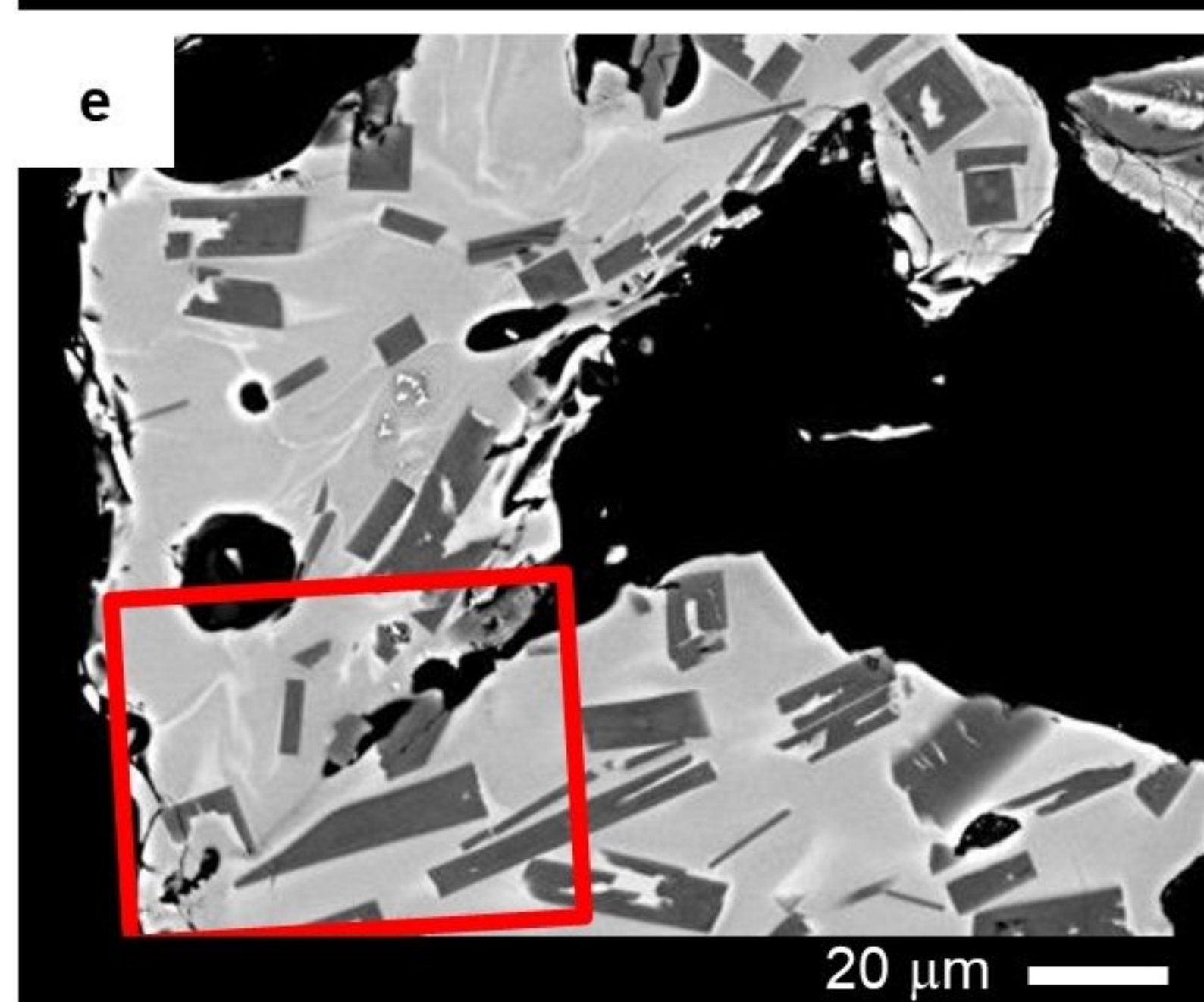
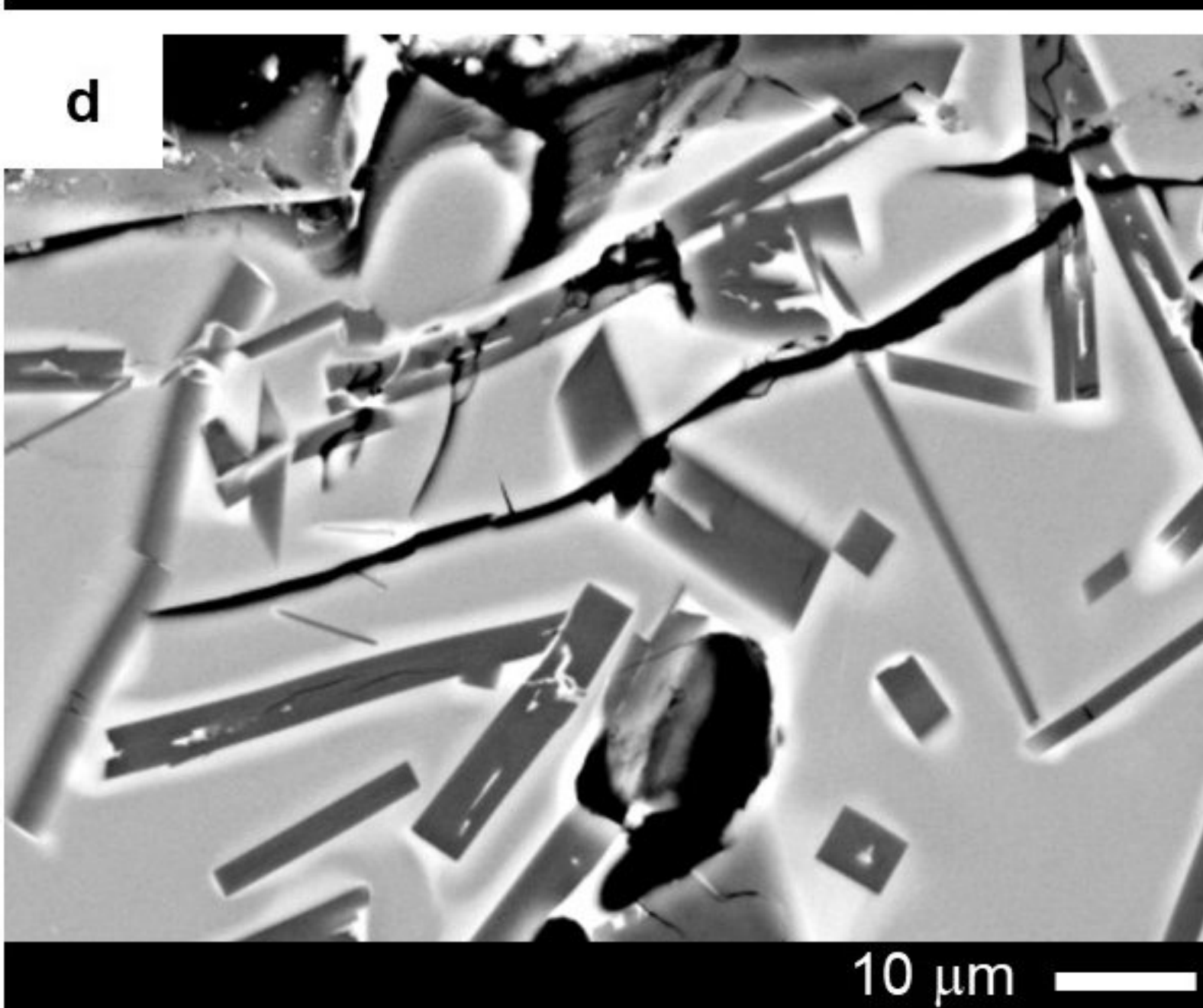
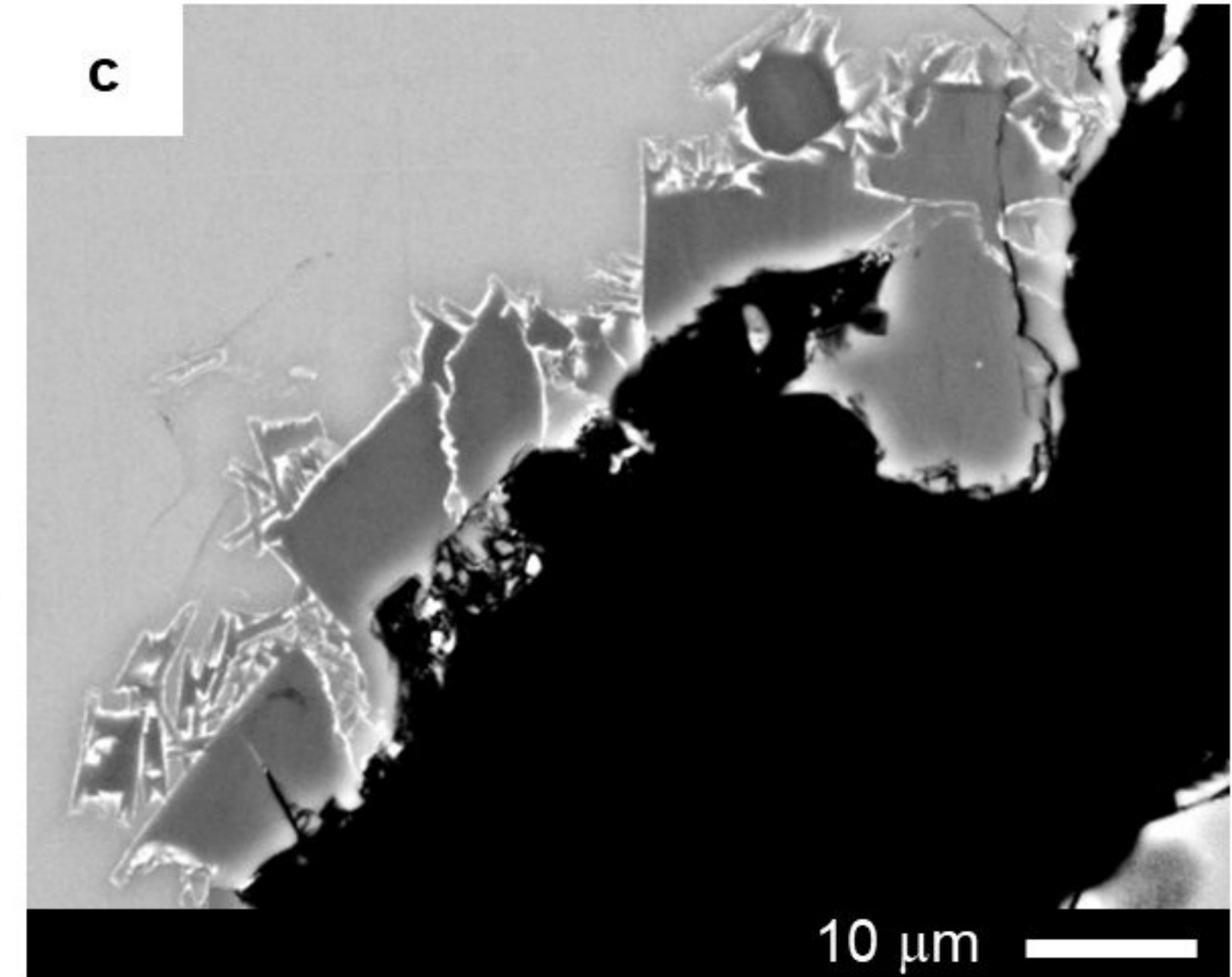
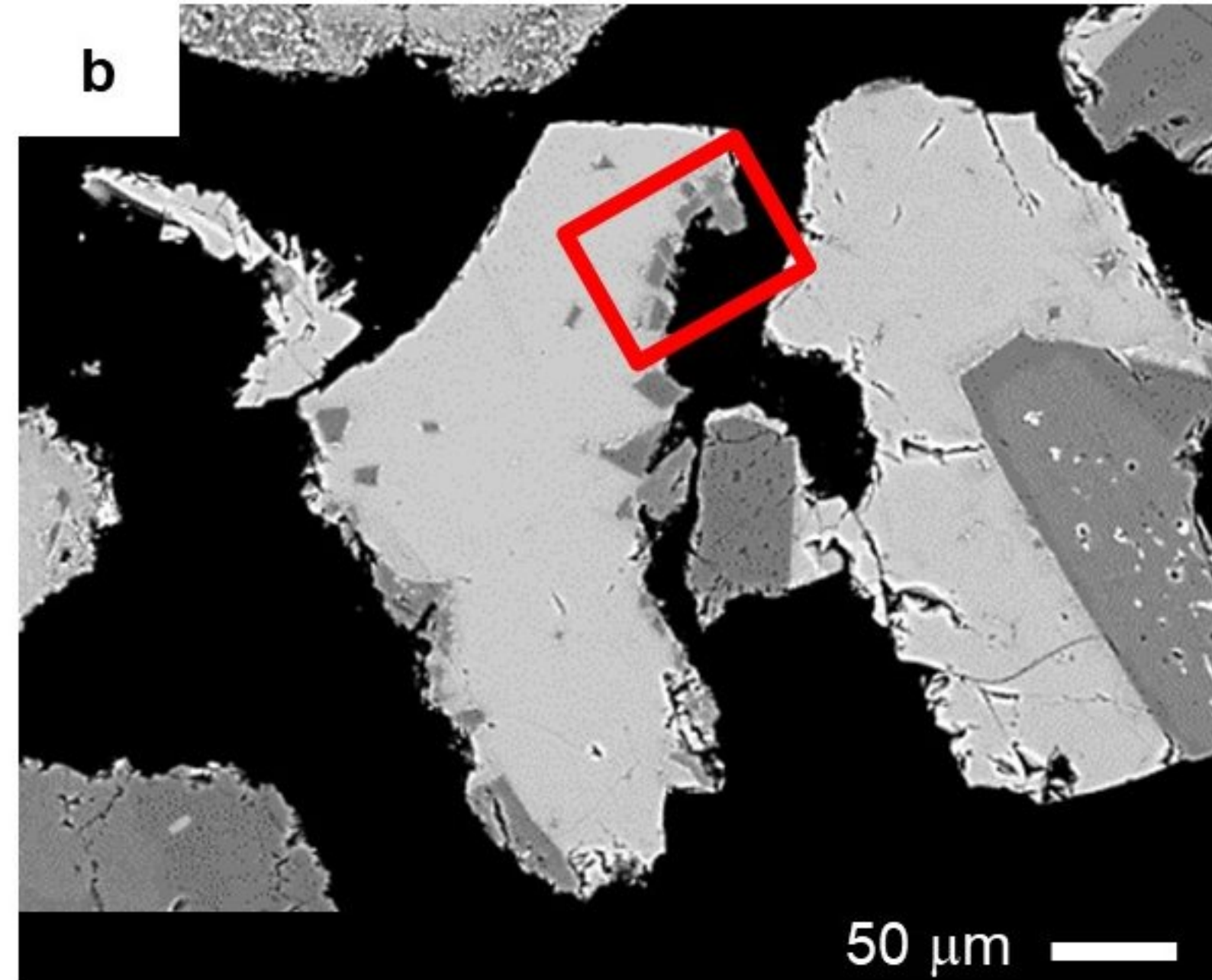
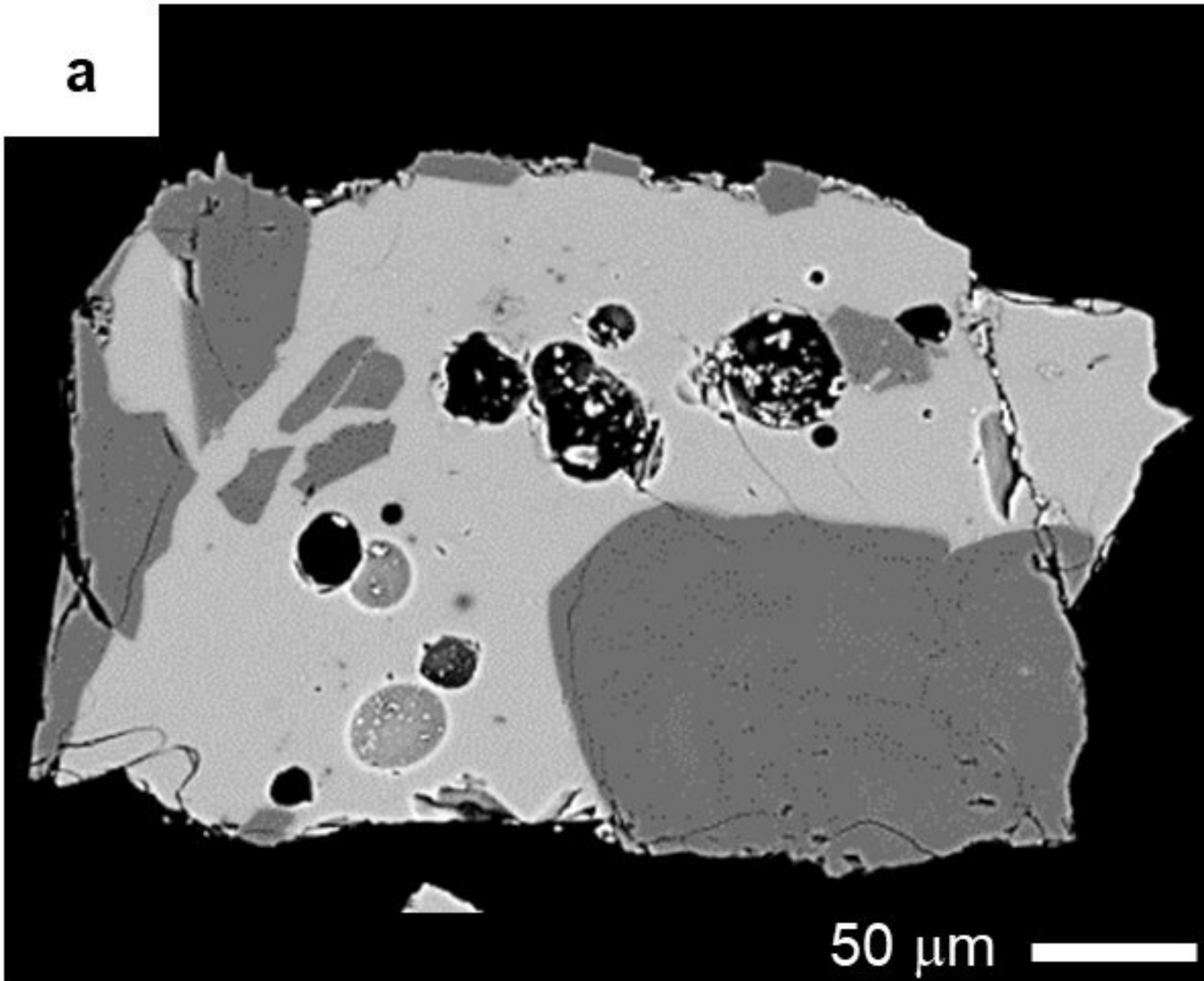
0  
0



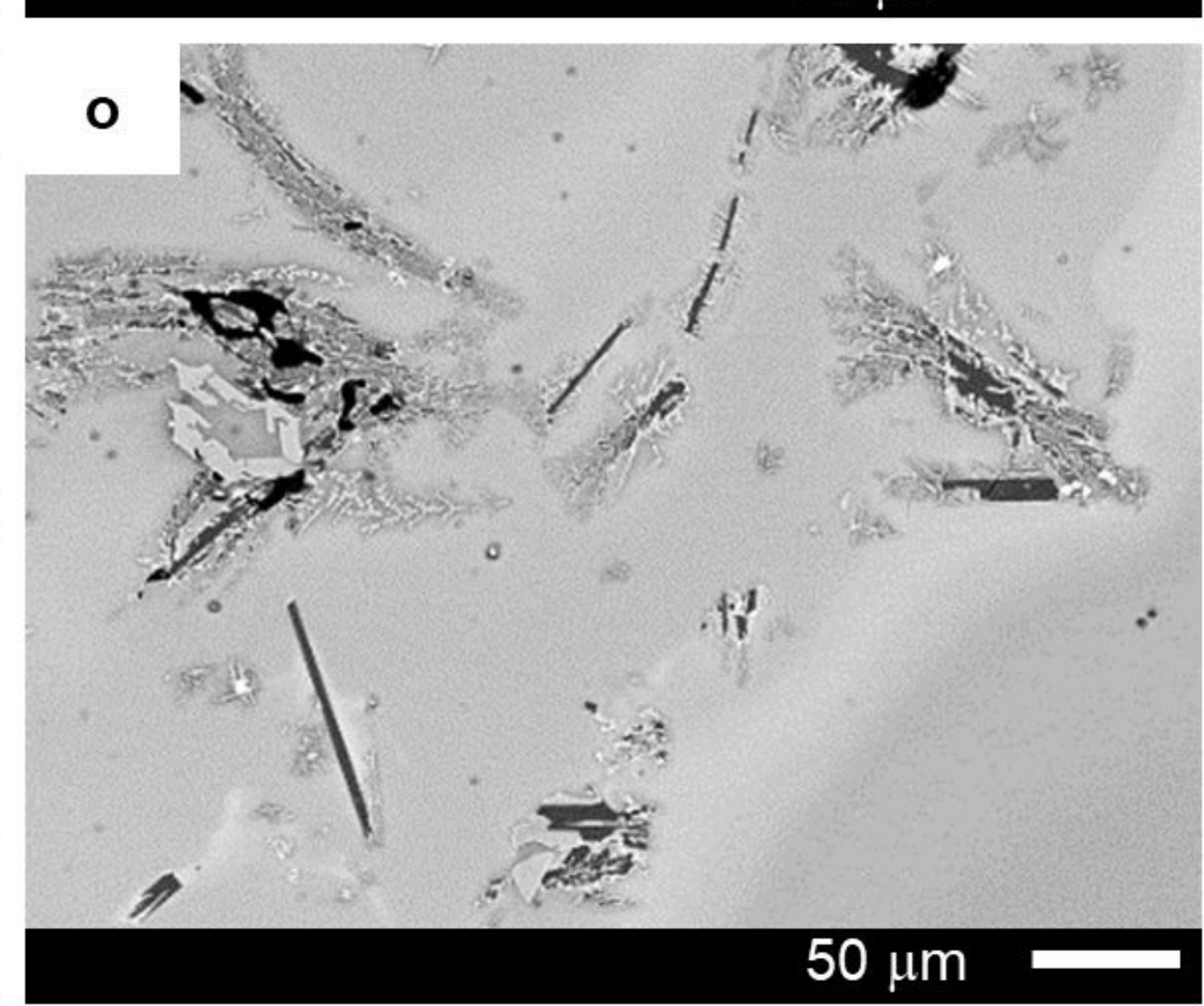
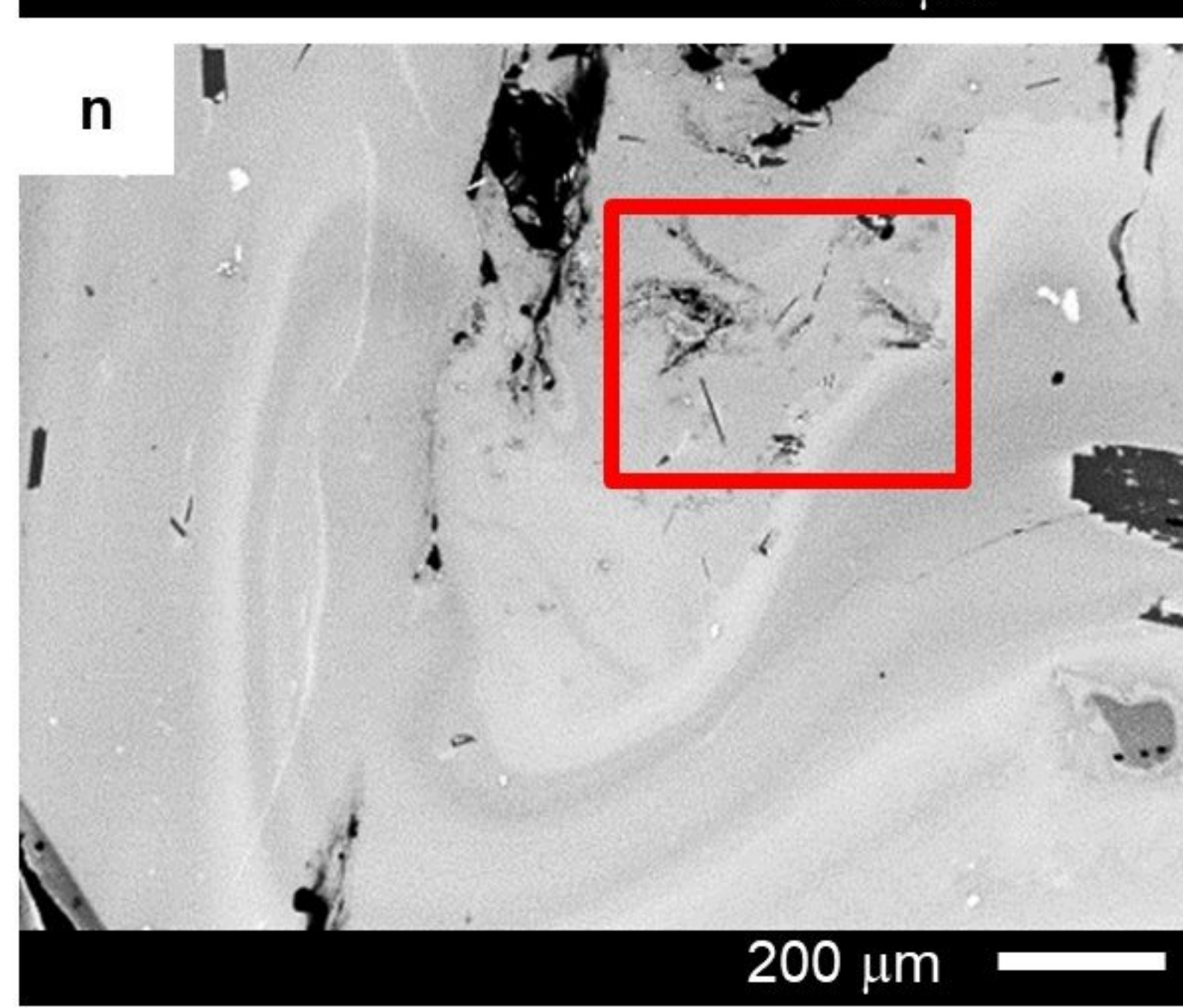
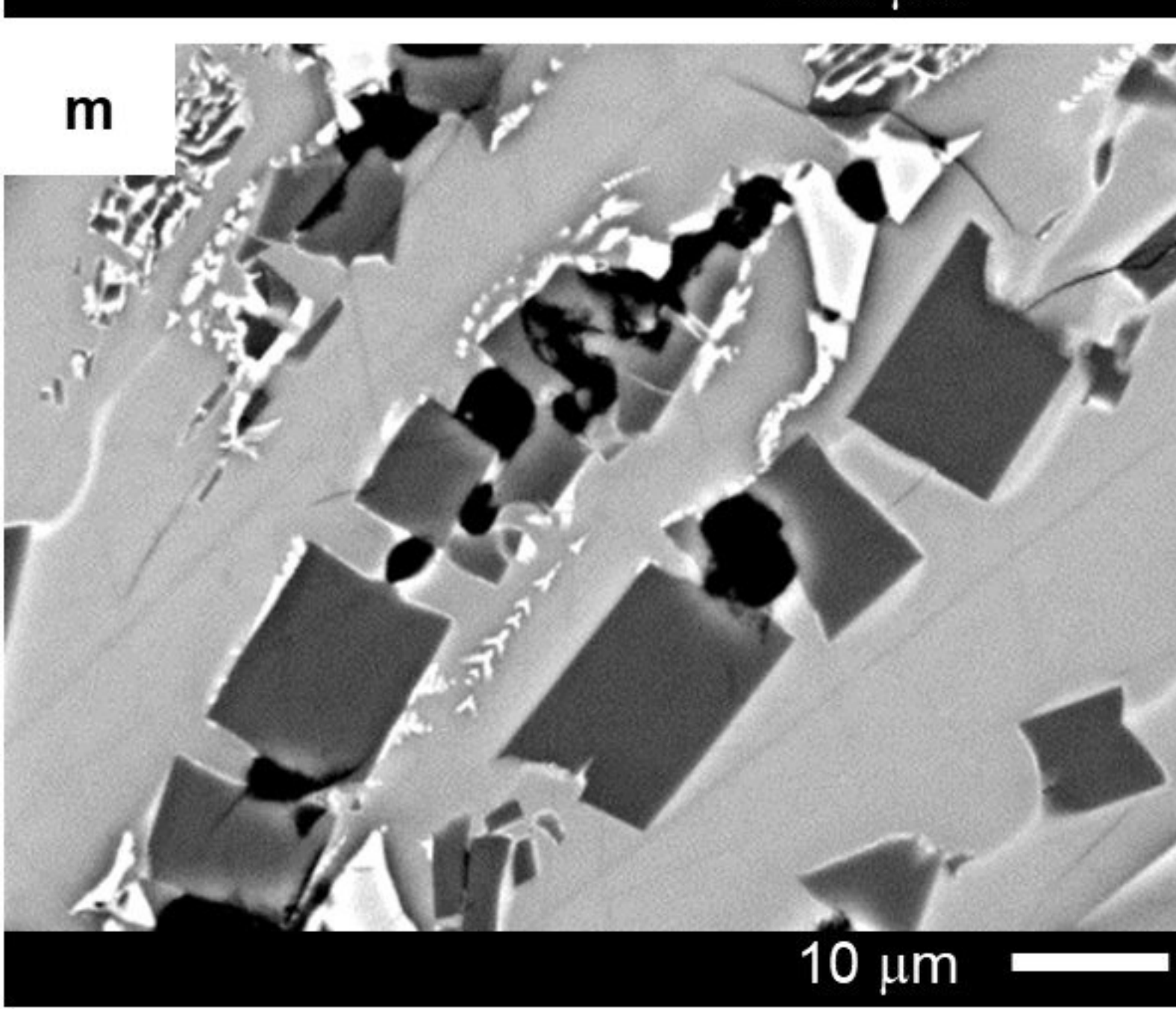
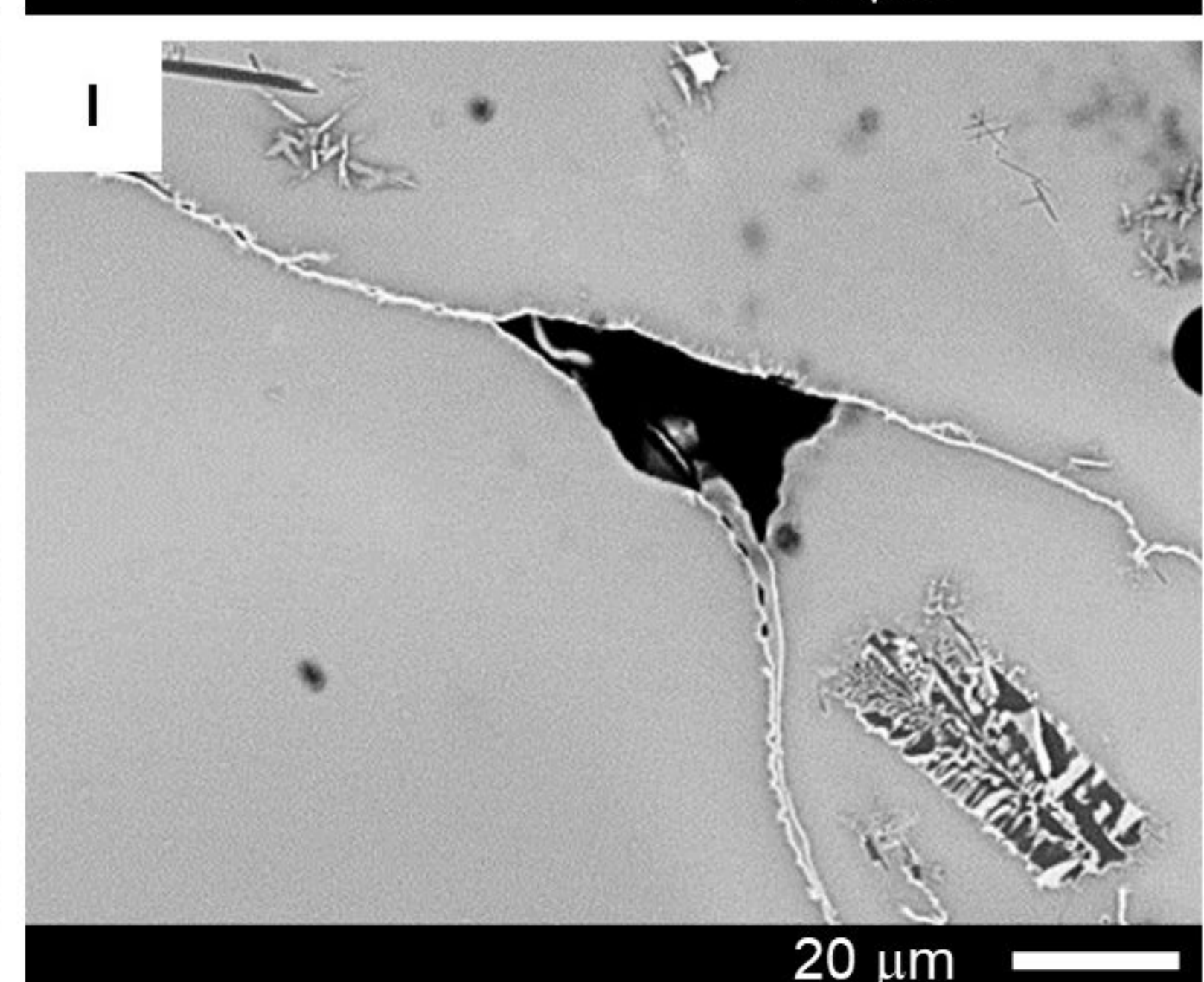
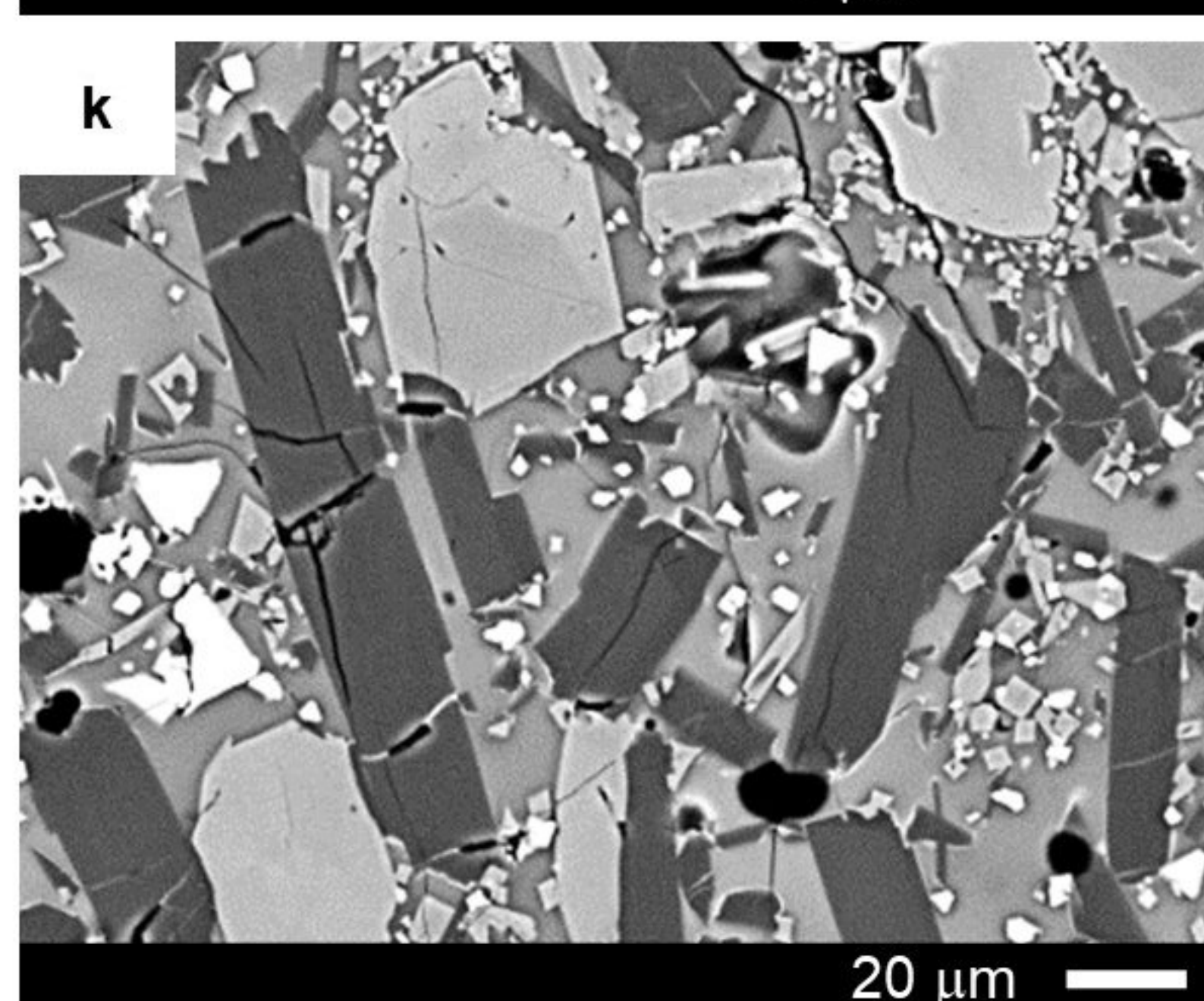
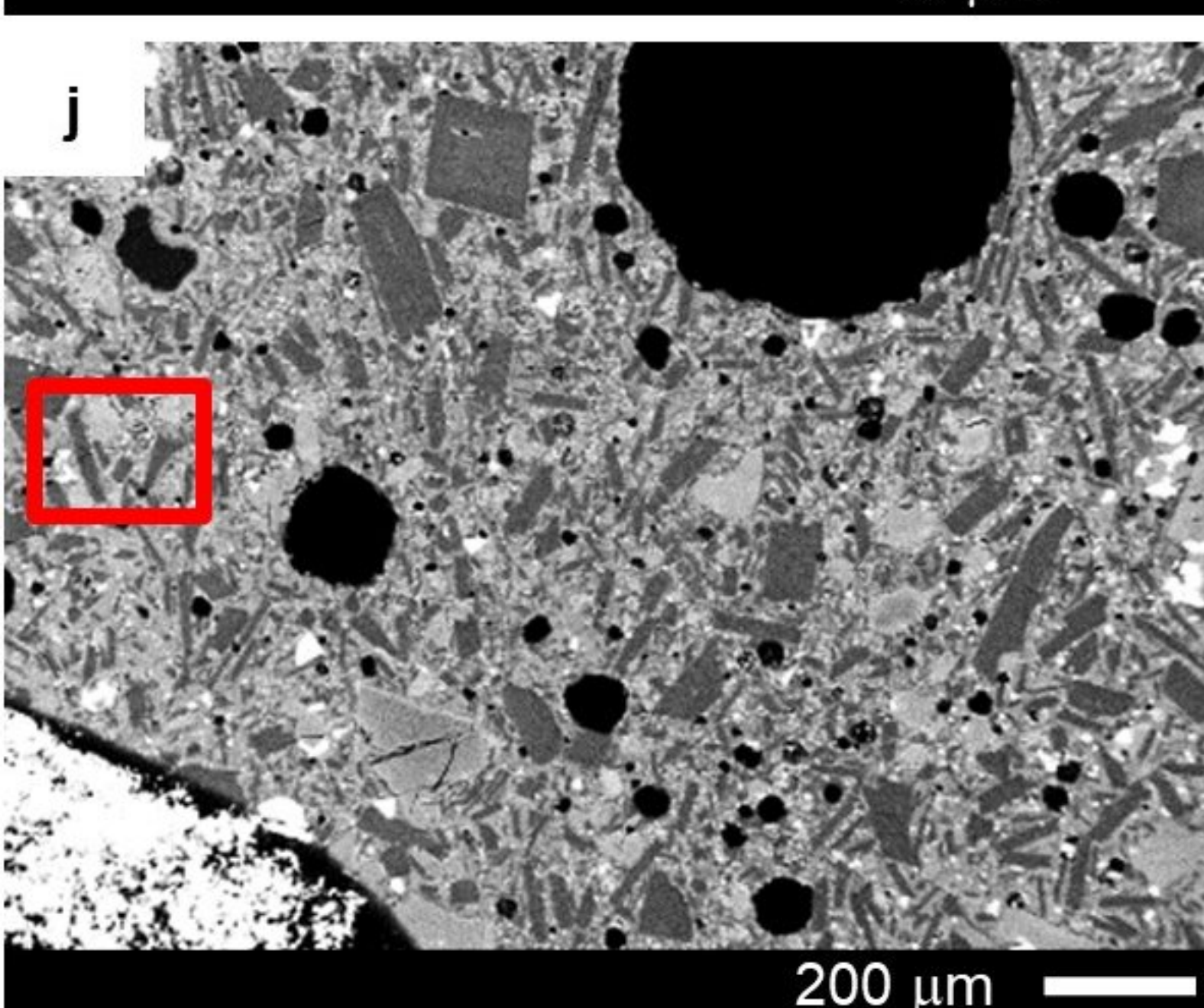
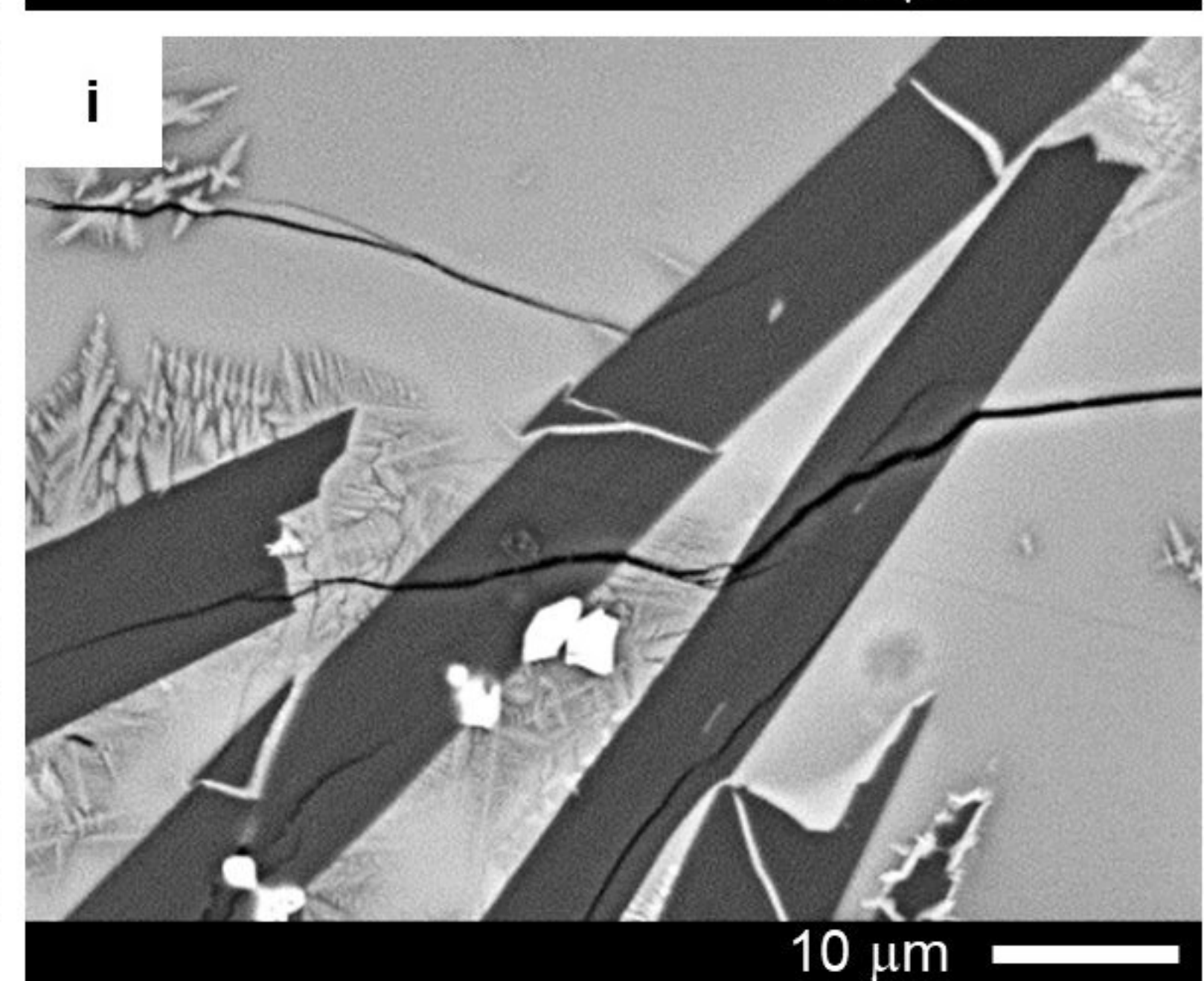
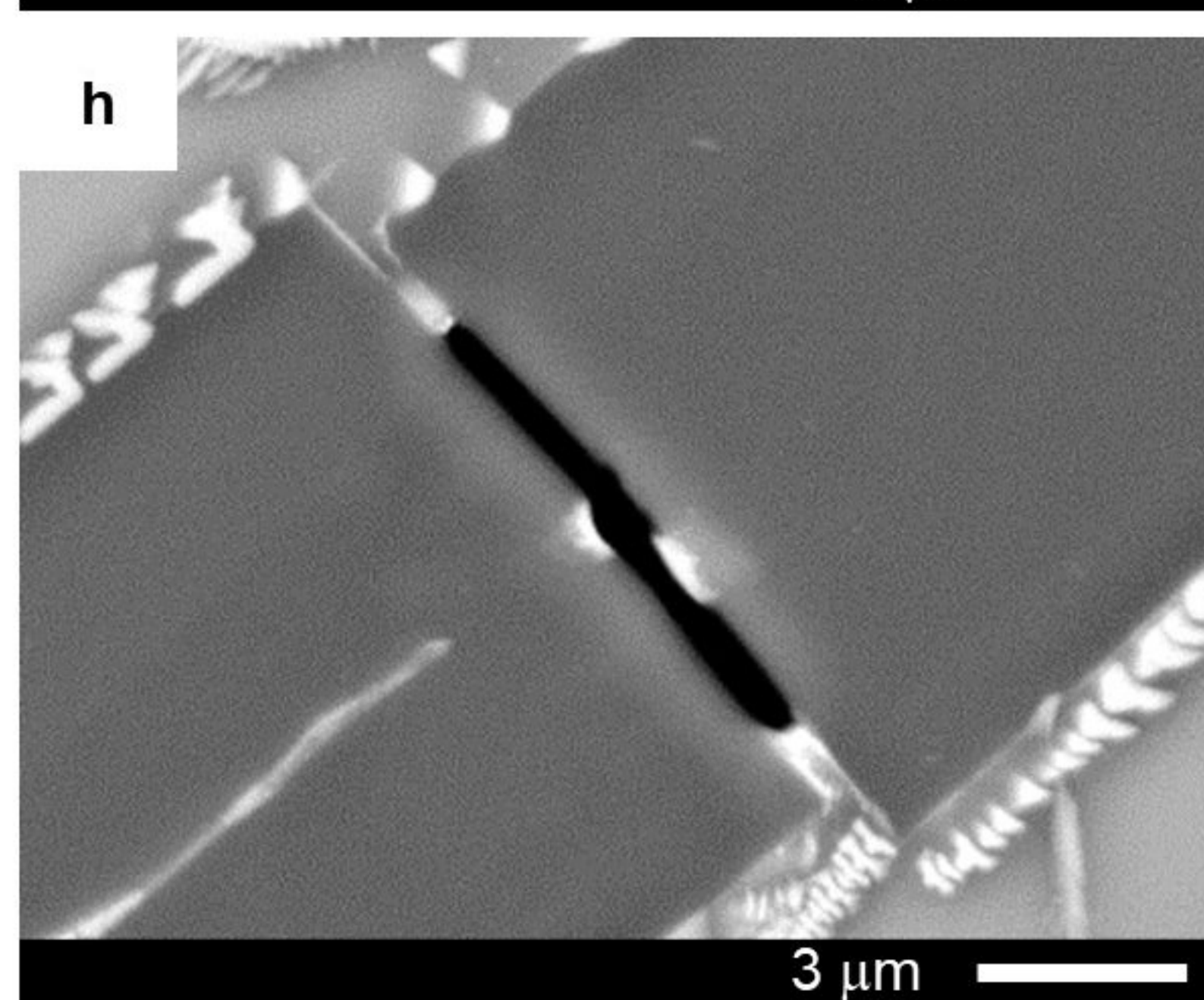
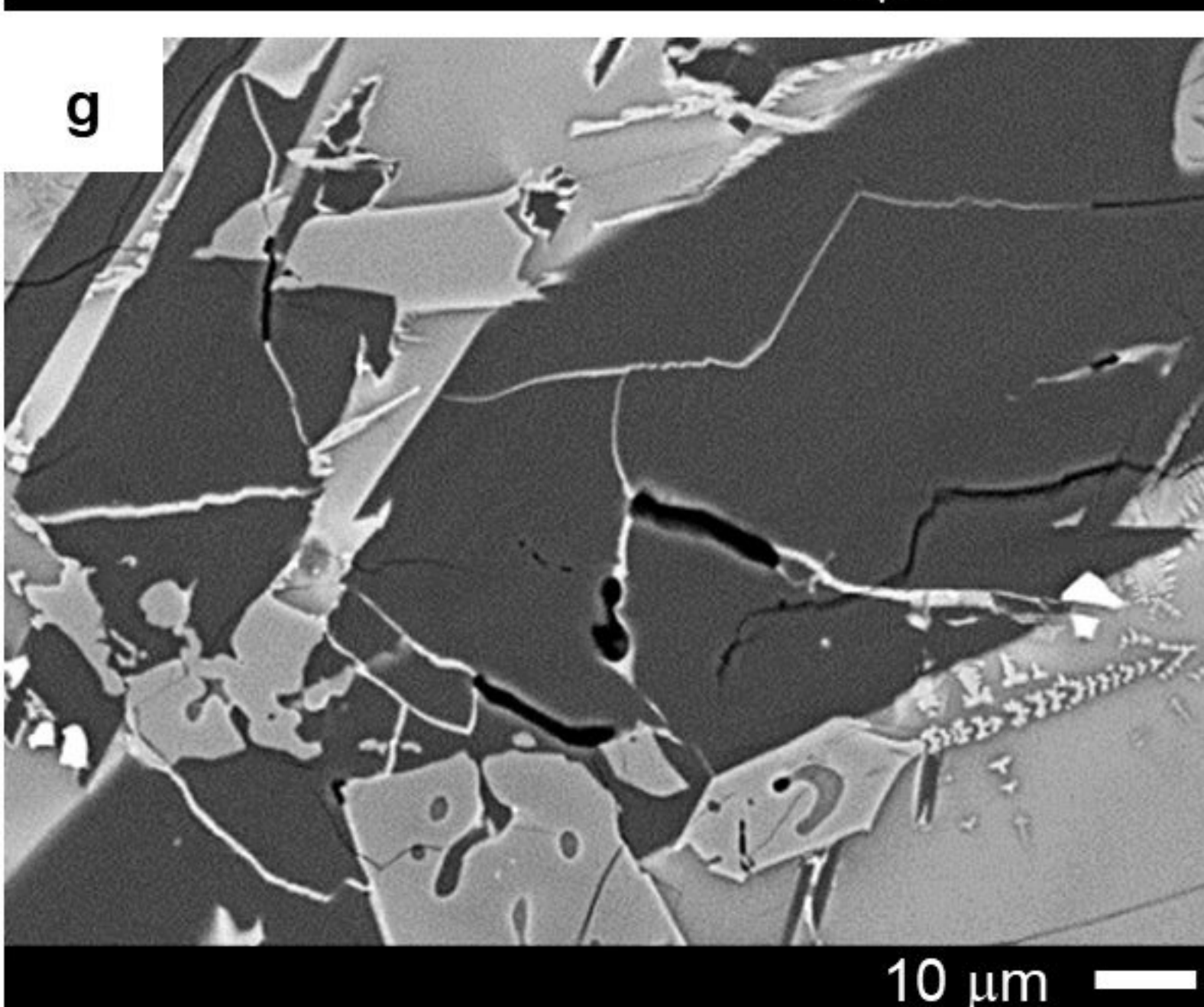
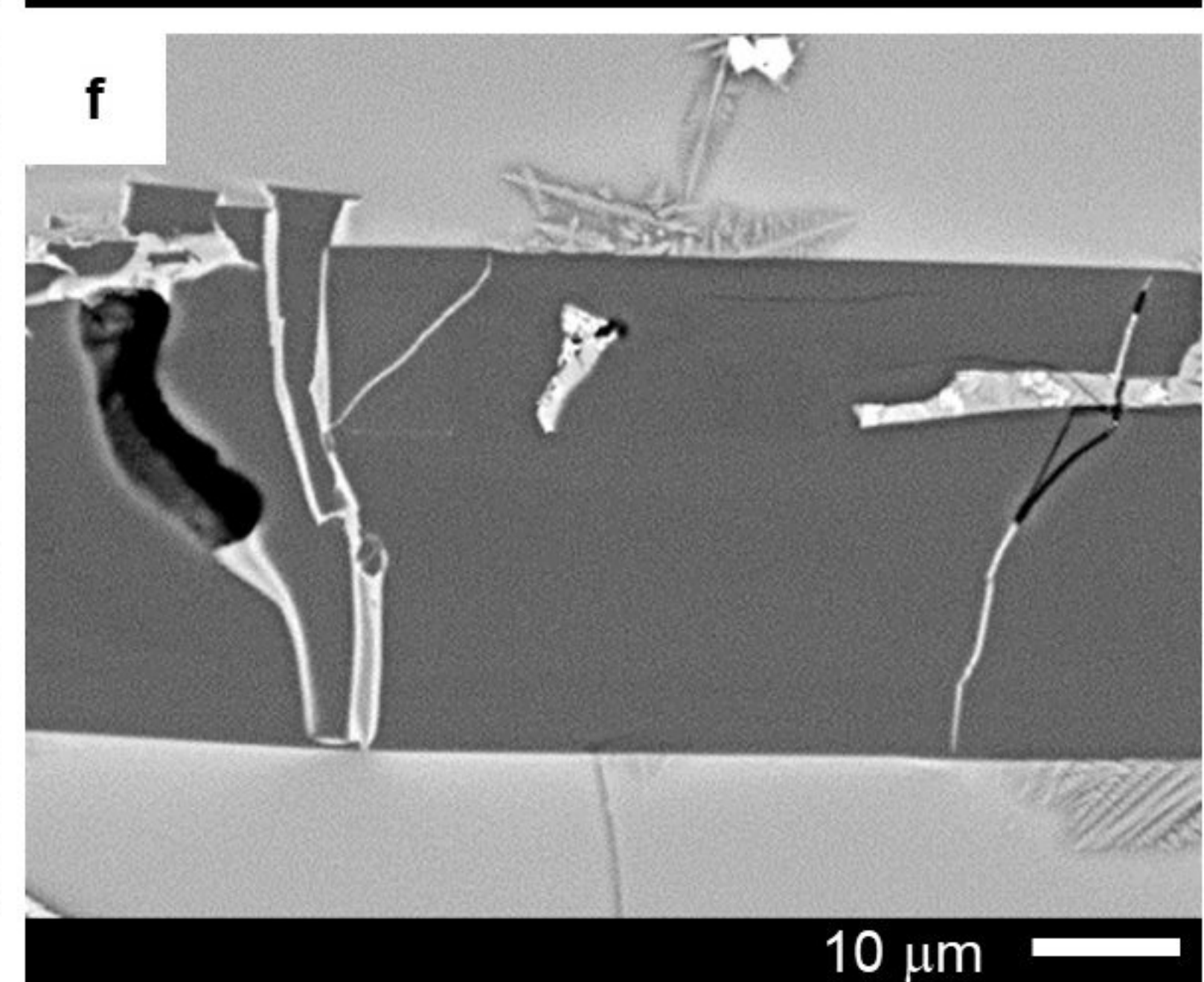
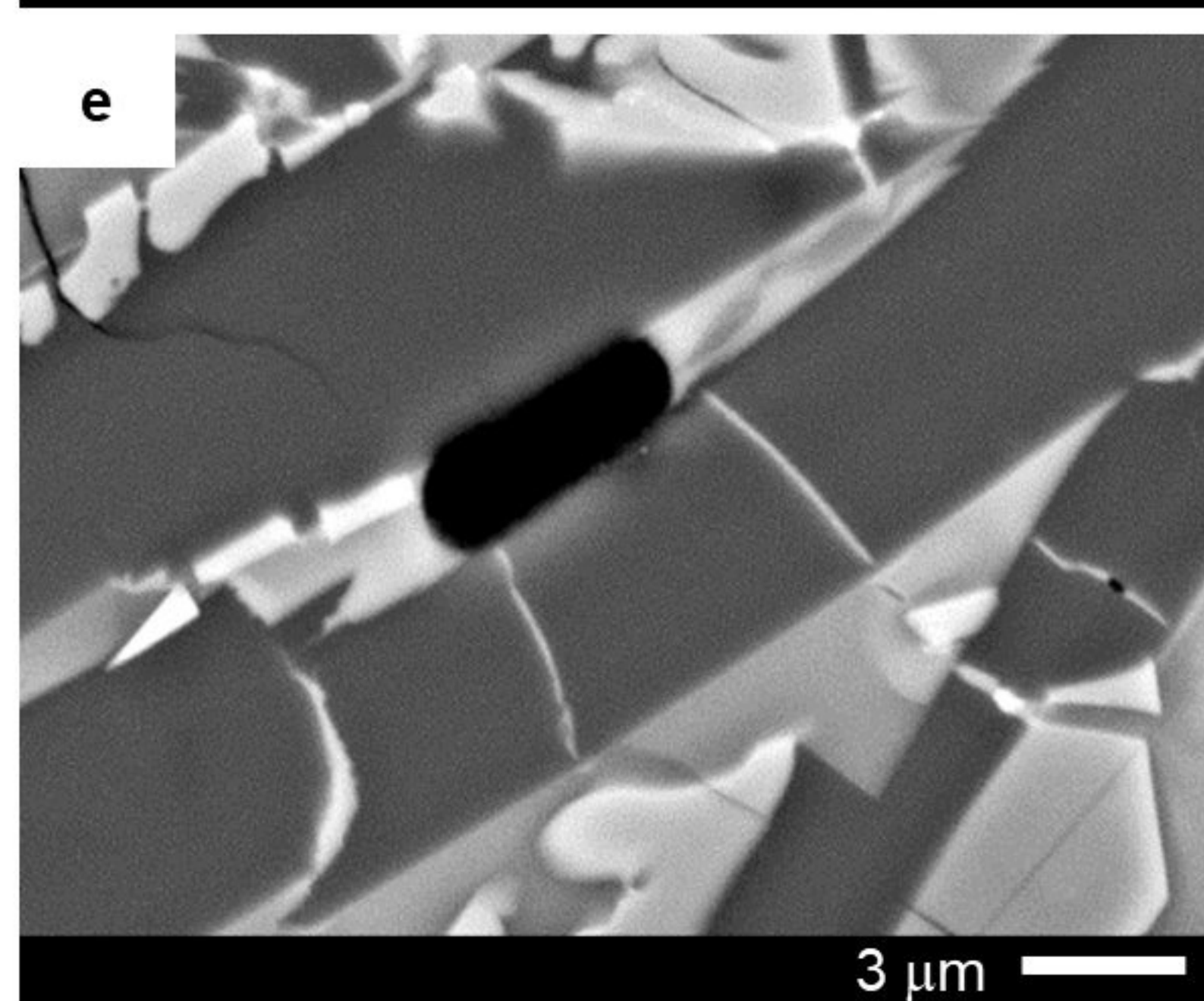
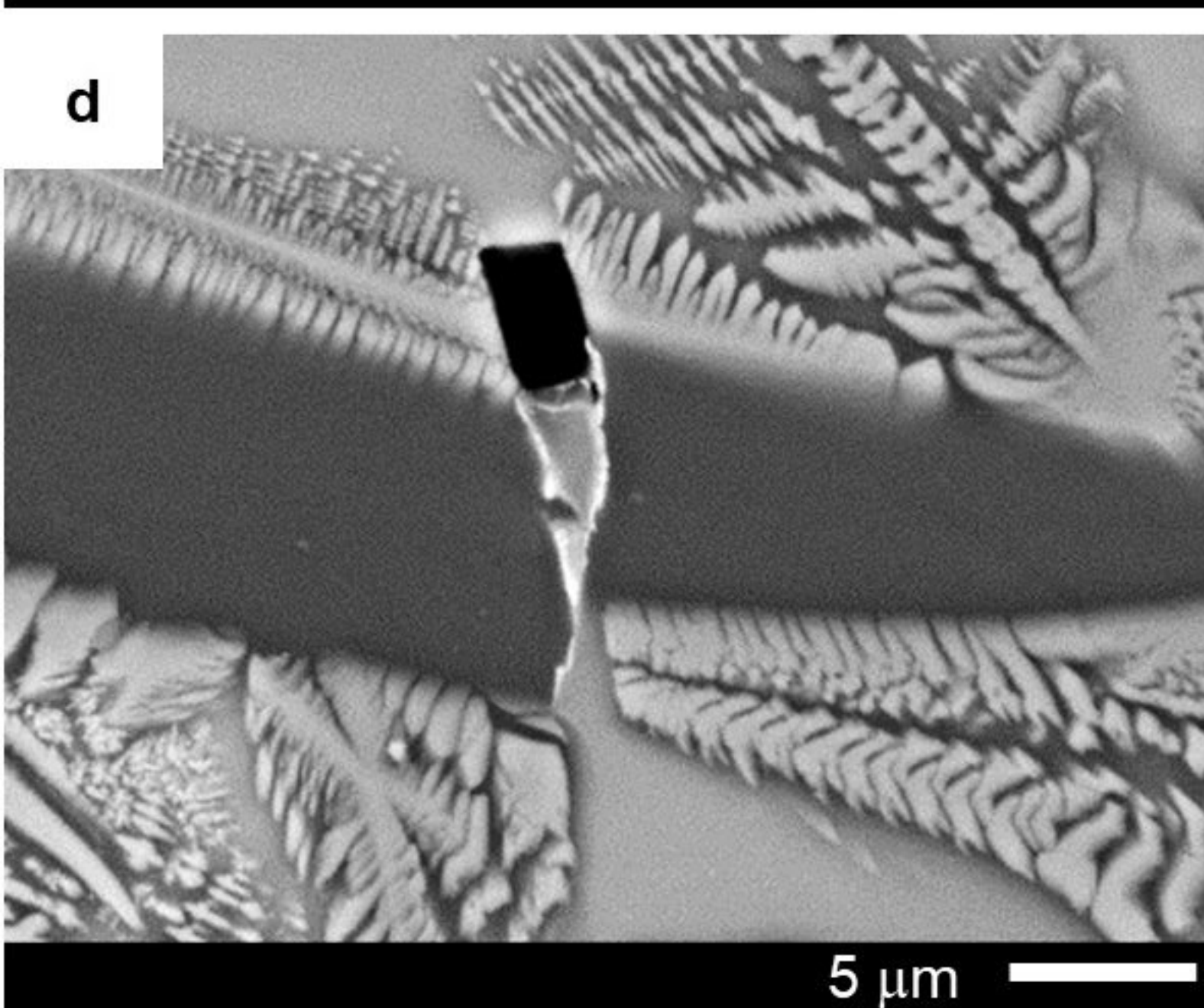
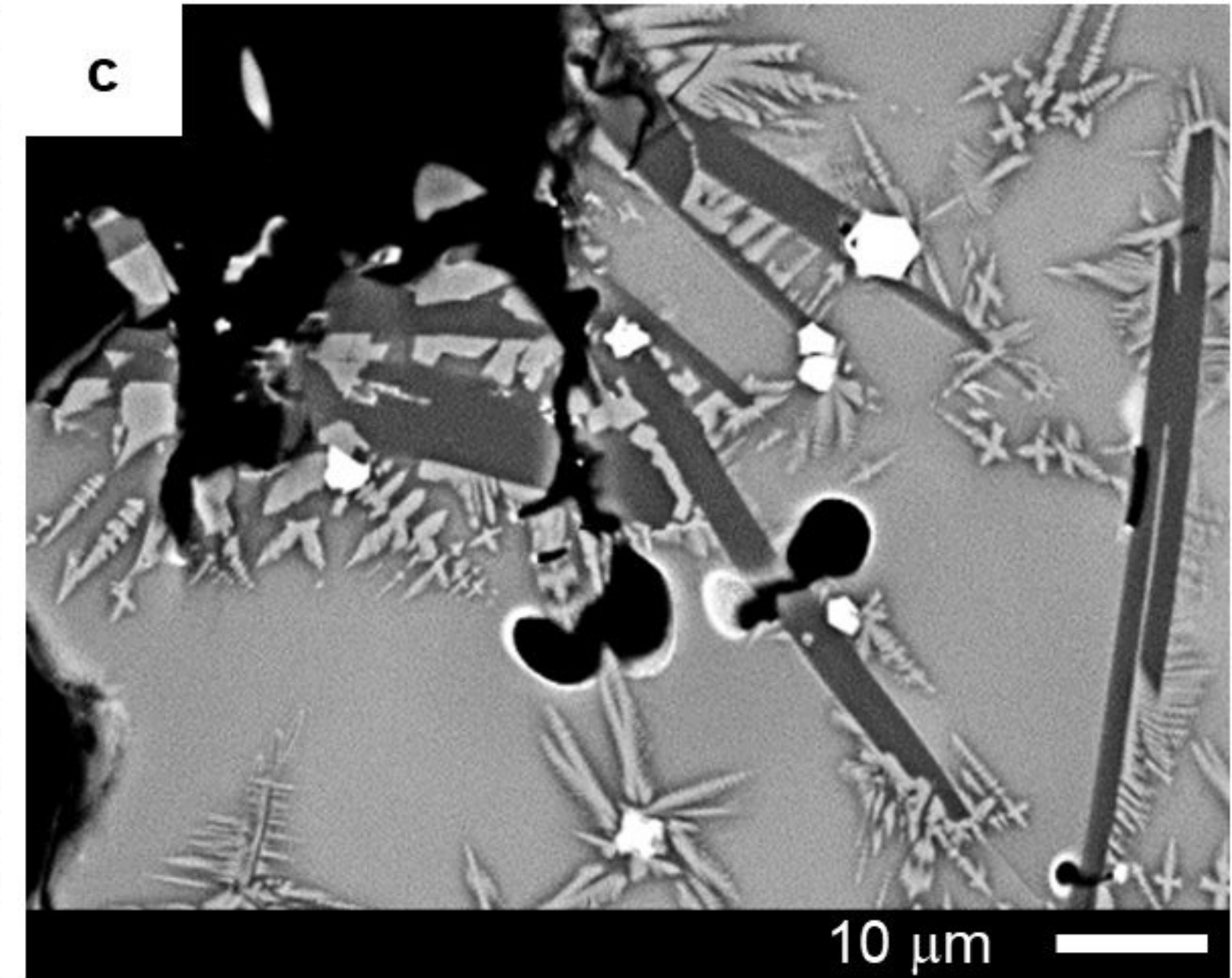
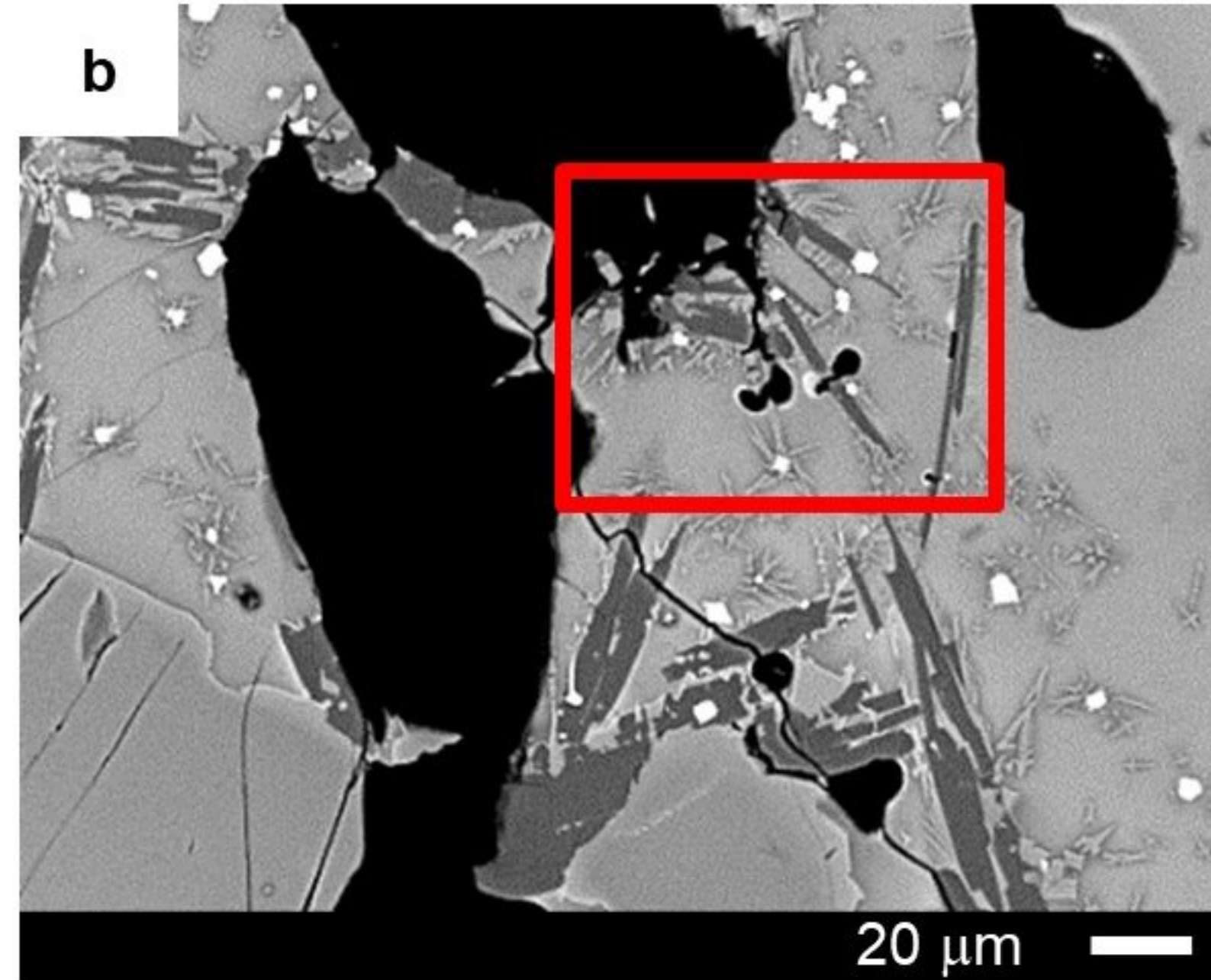
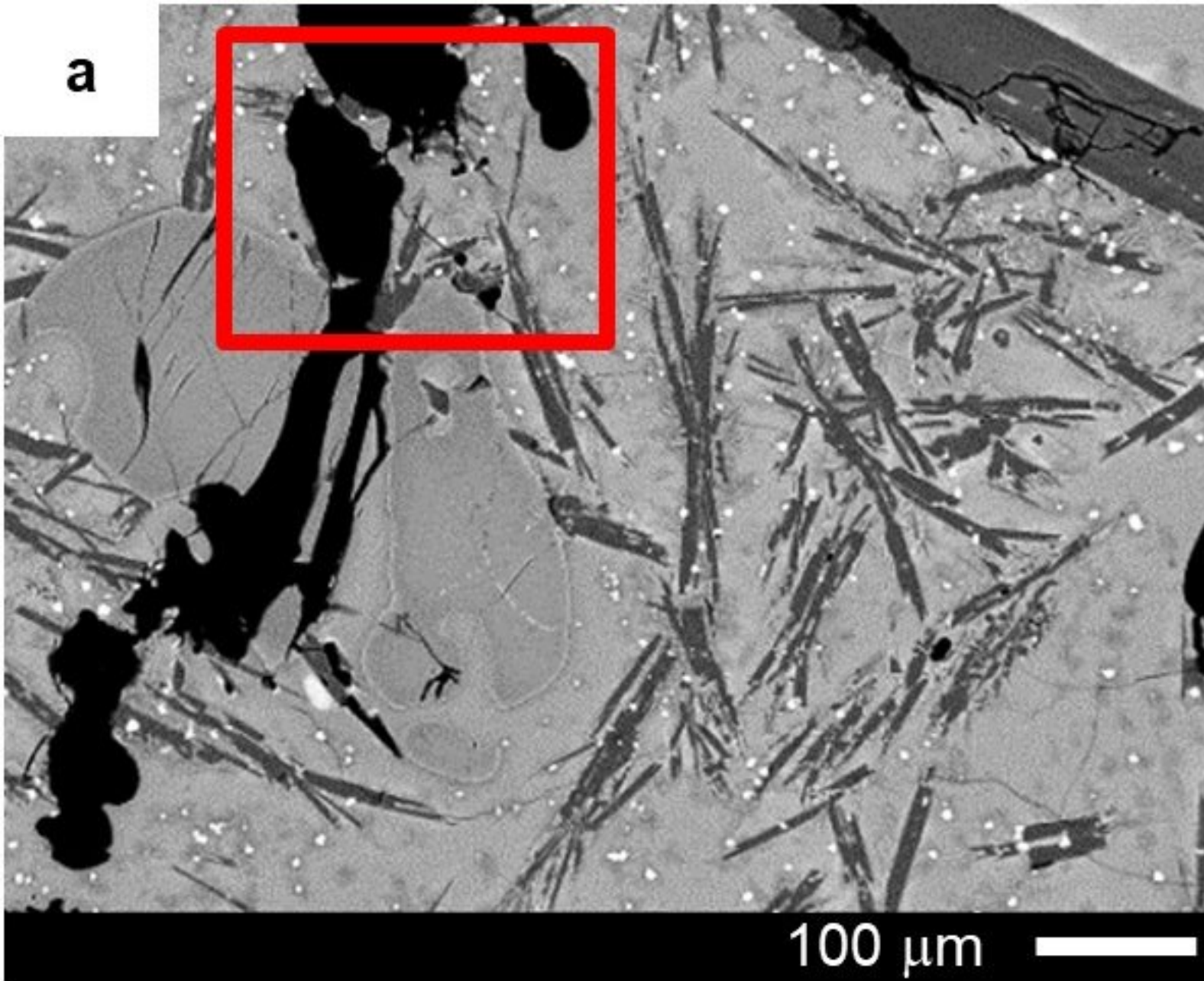
b













	glass (vol.%)	plagioclase (vol.%)	pyroxene (vol.%)	olivine (vol.%)	oxides (vol.%)	mafics* (vol.%)	crystallinity (vol.%)	references
<b>Experiment #</b>								
<b>6</b>	83.7 ± 12.0	4.4 ± 3.1	4.4 ± 3.1	3.1 ± 4.4	4.4 ± 6.3		16.3 ± 12.0	this work
<b>8</b>	63.6 ± 4.1	24.2 ± 2.2	4.0 ± 2.2	7.9 ± 5.4	0.4 ± 1.1		36.4 ± 5.1	this work
<b>9</b>	60.7 ± 8.1	29.8 ± 6.7	6.6 ± 10.4	1.9 ± 2.5	1.1 ± 1.5		39.3 ± 8.1	this work
<b>10</b>	37.1 ± 6.4	43.0 ± 3.9	11.8 ± 4.0	5.3 ± 2.7	2.5 ± 1.5		62.7 ± 6.2	this work
<b>11</b>	43.5 ± 9.2	38.6 ± 6.9	12.8 ± 4.1	4.2 ± 1.3	1.9 ± 0.7		57.6 ± 8.1	this work
<b>11a</b>	57.6 ± 10.6	23.2 ± 7.7	10.8 ± 16.5	6.4 ± 5.9	2.0 ± 2.0		42.4 ± 10.1	this work
<b>12</b>	58.4 ± 6.8	34.3 ± 7.0	2.9 ± 3.6	4.0 ± 2.8	0.4 ± 0.2		41.6 ± 6.8	this work
<b>13</b>	37.3 ± 6.2	34.0 ± 5.4	21.3 ± 3.3	4.3 ± 2.1	3.4 ± 0.5		63.0 ± 6.1	this work
<b>13a</b>	56.0 ± 10.5	27.5 ± 8.1	7.8 ± 14.7	7.9 ± 3.2	0.7 ± 0.5		44.0 ± 10.4	this work
<b>15</b>	49.0 ± 8.3	30.9 ± 2.1	11.8 ± 8.0	6.7 ± 4.0	1.6 ± 1.7		51.0 ± 8.3	this work
<b>17</b>	97.0 ± 2.0	2.9 ± 1.9	0.0 ± 0.1	0.1 ± 0.3	0.0 ± 0.0		3.0 ± 2.0	this work
<b>Eruption</b>								
<b>Etna 2001</b>	60.4 ± 4.2	25.1 ± 2.8	10.1 ± 5.5	1.6 ± 1.0	2.9 ± 0.8		39.6 ± 4.2	this work
<b>Etna 2002</b>	45.6	31.4	17.1	2.7	3.2		54.4	this work
<b>Paricutin 1943</b>	60.9 ± 5.1	34.1 ± 4.4				4.9 ± 1.7	39.1 ± 5.1	this work
<b>Xitle 2 ka</b>	66.9 ± 7.9	29.3 ± 6.9				3.8 ± 2.1	33.1 ± 7.9	this work
<b>Croscat 11 ka</b>	98-57						2-43	61

\*Sum of pyroxene, olivine, and oxides. All values are the mean of >5 image measurements over 1-5 clasts, ± 1 standard deviation (except Etna 2002, one image only).